

Modeling of neutral particle transport at the W7-X divertor with COMSOL

Bachelor Thesis in Mechanical Engineering

Markus Grasser

31.01.2025

Reviewer: Prof. Dr.-Ing. Thomas Lex

Second Reviewer: Prof. Dr.-Ing. Thomas Schaeffer

Supervisor: Dr. Thierry Kremeyer



MAX PLANCK INSTITUTE
FOR PLASMA PHYSICS



OSTBAYERISCHE
TECHNISCHE HOCHSCHULE
REGENSBURG

“Finally I got to carbon, and as you all know, in the case of carbon the reaction works out beautifully. One goes through six reactions, and at the end one comes back to carbon. In the process one has made four hydrogen atoms into one of helium. The theory, of course, was not made on the railway train from Washington to Ithaca ... It didn’t take very long, it took about six weeks, but not even the Trans-Siberian railroad has taken that long for its journey.”

~ Hans Bethe



ERKLÄRUNG ZUR BACHELORARBEIT VON


Name: Grasser

Vorname: Markus

Studiengang: Bachelor Maschinenbau

1. Mir ist bekannt, dass dieses Exemplar der Bachelorarbeit als Prüfungsleistung in das Eigentum der Ostbayerischen Technischen Hochschule Regensburg übergeht.
2. Ich erkläre hiermit, dass ich diese Bachelorarbeit selbständig verfasst, noch nicht anderweitig für Prüfungszwecke vorgelegt, keine anderen als die angegebenen Quellen und Hilfsmittel benutzt sowie wörtliche und sinngemäße Zitate als solche gekennzeichnet habe.

Regensburg, den 22.01.2025


.....
Unterschrift

Diese Erklärung ist mit der Bachelorarbeit (eingehftet) abzugeben.

Abstract

This thesis presents a simplified model of the neutral particle transport at the divertor of the Wendelstein 7-X stellarator. The model uses the angular coefficient method implemented in the commercial software COMSOL Multiphysics to calculate the neutral particle transport as a free molecular flow. The location of the neutral particle origin is derived by coupling the simulation to the plasma edge code EMC3-Lite. The presented simulation is capable of quantifying the amount of reionised particles, the particle flux entering the sub-divertor region and the contribution of different wall components to the neutral particle transport in a few CPU minutes. A preliminary validation of the simulation shows that the results are comparable to experimental and EMC3-Eirene values.

Kurzzusammenfassung

In dieser Arbeit wird ein vereinfachtes Modell des Neutralteilchentransports am Divertor des Stellarators Wendelstein 7-X vorgestellt. Das Modell verwendet die “Angular Coefficient”-Methode, die in der kommerziellen Software COMSOL Multiphysics implementiert ist, um den Neutralteilchentransport als molekulare Strömung zu berechnen. Der Ort der Neutralteilchenentstehung wird durch Kopplung der Simulation mit dem Plasmarandschichtcode EMC3-Lite bestimmt. Die vorgestellte Simulation ist in der Lage, die Menge der reionisierten Teilchen, den in den Subdivertorraum eintretenden Teilchenfluss und die Beteiligung der verschiedenen Wandkomponenten am Neutralteilchentransport in wenigen CPU-Minuten zu quantifizieren. Eine vorläufige Validierung der Simulation zeigt, dass die Ergebnisse mit experimentellen Werten und den Simulationswerten von EMC3-Eirene vergleichbar sind.

Contents

1	Introduction	1
2	Theoretical Background	3
2.1	Thermonuclear fusion	3
2.2	Magnetic confinement	5
2.3	Divertor function and relevance	7
2.3.1	Plasma-wall interaction	8
2.3.2	Heat and particle exhaust	9
2.3.3	Plasma-neutrals interaction	12
2.3.4	Island divertor concept	13
2.4	Wendelstein 7-X	15
2.4.1	Divertor configuration	16
2.4.2	Neutral particle transport	19
2.5	Rarefied flow regimes	21
2.5.1	Knudsen number	21
2.5.2	Lambert's cosine law	23
2.5.3	AC Method	24
3	Current transport codes and motivation	26
4	Development of simplified neutral particle transport simulation	28
4.1	Deterministic approach	28
4.2	Kisslinger file format	29
4.3	Geometry	30
4.4	Meshing	32
4.5	Resolution optimum	35
4.6	EMC3-Lite coupling	36
4.7	Boundary conditions	39
4.8	Results	41
4.8.1	Standard configuration	42
4.8.2	High-iota configuration	44
4.8.3	High-mirror configuration	46
4.9	Validation	48
4.10	Improvement possibilities	49
5	Summary	51

1 Introduction

In recent decades, global climate change has emerged as one of the major challenges of the 21st century. While public awareness and political action on the issue are growing, the statistics report negative records. In 2023, global warming led to a peak in global mean sea level, glacier retreat, antarctic sea-ice loss and greenhouse gas concentrations. In the same year, the Paris Agreement's goal of limiting global surface temperature increase to 1.5°C came close to being exceeded, at a value of 1.45°C [1].

The energy sector is currently the largest source of emissions and appears to be on a positive trend. In 2023, the share of fossil fuels in global primary energy production was 81.5 %, a decrease of 0.4 % compared to the previous year. The global amount of electricity generated from renewables increased by 1 % to 30 %. Nevertheless, the absolute level of greenhouse gas emissions reached an all-time high of 40 gigatonnes [2]. In order to combat climate change and its consequences, a shift from fossil fuels to renewable, emission-free energy is needed. While renewable energy sources do not produce emissions, their energy output is highly dependent on environmental factors and therefore cannot provide a constant supply of energy. One promising candidate for solving this problem is energy production through thermonuclear fusion in a so-called fusion reactor [3].

The relevance of nuclear fusion is demonstrated by the international research effort. After the first theoretical descriptions of nuclear fusion in the 1920s and 1930s, the first ideas about using this process for energy production were proposed in the 1950s. Since then, there has been strong international collaboration. The first major international fusion experiment was the Joint European Torus (JET), which was completed in 1983. This research reactor still holds the record for the highest energy produced in a civil fusion reaction, at 69 MJ [4]. The next major milestone was the agreement by the European Union, the United States, the Soviet Union and Japan (later also South Korea, China and India) to jointly design the International Thermonuclear Experimental Reactor (ITER), which has been under construction since 2010 in Cadarache, France [5]. ITER is designed to produce 500 MW of fusion power with an injected power of 50 MW. As its name suggests, it is still a research reactor and will not be used to generate electricity for the grid. In 2018, EUROfusion,

an international fusion research consortium, published a roadmap [6] outlining the timetable from now until the first commercial fusion power plant. According to this roadmap, the first experiments at ITER were supposed to be carried out in the year 2025. Due to technical difficulties, this date has been postponed to 2034 [7]. The roadmap foresees that the results from ITER and other research institutes will lead to the development of the demonstration fusion power plant DEMO, for which the design process is already underway. Successful operation of DEMO is expected to pave the way for commercial fusion power plants. A limiting factor in fusion research is the immense cost of the experiments. Over the years, the estimated cost of ITER has risen to around €25 billion [8]. A positive change in the fusion research landscape is the increased founding of private companies. Up to 2024, around 45 private companies are working on the exploitation of fusion energy. Cumulative investment in the private sector is approximately \$7 billion [9].

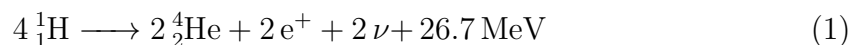
The most technologically advanced approaches to fusion power plants are tokamaks and stellarators. Despite significant progress in their research, several challenges remain, such as efficient plasma heating and confinement, the development of advanced materials, tritium breeding, and heat and particle exhaust [3]. This thesis addresses the latter challenge by presenting a simplified simulation of neutral particle transport at the divertor of the Wendelstein 7-X stellarator. The thesis is structured as follows: In Section 2, the theoretical background of magnetic confinement fusion, plasma edge and divertor physics, the Wendelstein 7-X and rarefied flow regimes is discussed. Then, current transport codes used to simulate heat and particle transport at the divertor are presented in Section 3. Section 4 describes the necessary steps for the simplified simulation with COMSOL Multiphysics (COMSOL). Finally, Section 5 summarises the results and gives an outlook on future work based on the simplified simulation.

2 Theoretical Background

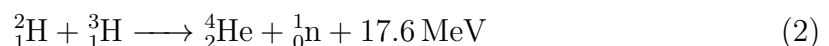
2.1 Thermonuclear fusion

Thermonuclear fusion is the process of merging atomic nuclei at very high temperatures. High temperatures are needed to overcome the Coulomb barrier repelling atomic nuclei from each other. During the fusion of light atomic nuclei, large amounts of energy are released due to the change of the nuclear binding energy. The energy density of these nuclear reactions is millions of times greater than that of chemical reactions, so that one gram of fused hydrogen produces the energy of around 11 tons of burnt coal [10]. Research into how to harness this process for civilian energy production has been going on for several decades. The main advantages of fusion energy are the absence of greenhouse gas emissions, the abundance of fuel and independence from external factors such as solar radiation and wind speed. Fusion reactors do not produce long-lasting radioactive waste and there is no risk of nuclear disasters as with fission reactors [11]. Up to now, the conditions for a fusion power plant with net energy gain have not been met.

Nuclear fusion is the natural process responsible for the energy production of stars. Under stellar conditions, the hydrogen isotope protium fuses to helium in several steps. This reaction is very unlikely to occur and is therefore not suitable for terrestrial energy production. The net equation is:



The fusion reaction with the highest cross section is that of the hydrogen isotopes deuterium and tritium to helium. The majority of fusion research is focused on carrying out this reaction [12].



An important benchmark for fusion reactions is the energy gain factor Q . It describes the ratio of generated fusion energy to the heating energy required to achieve the reaction. $Q = 1$ is known as scientific break-even. This threshold defines the so-called ignition, after which the fusion reaction is self-sustaining and therefore "burns"

without external heating. The extreme conditions required for scientific break-even are quantified by the fusion triple product, consisting of density, temperature and confinement time. $Q = 1$ is reached at a fusion product of around $3 \cdot 10^{21} \frac{\text{keV}\cdot\text{s}}{\text{m}^3}$ [13]. Figure 1 shows the progress of fusion research for different approaches as measured by the fusion product. Note that the fusion product is scaled logarithmically. As the figure shows, the milestone of scientific break-even was reached in 2022 by the National Ignition Facility with a Q-factor of 1.54 [14]. The highest man-made fusion energy gain was reached by the Tsar Bomba with $Q \approx 30$ [15].

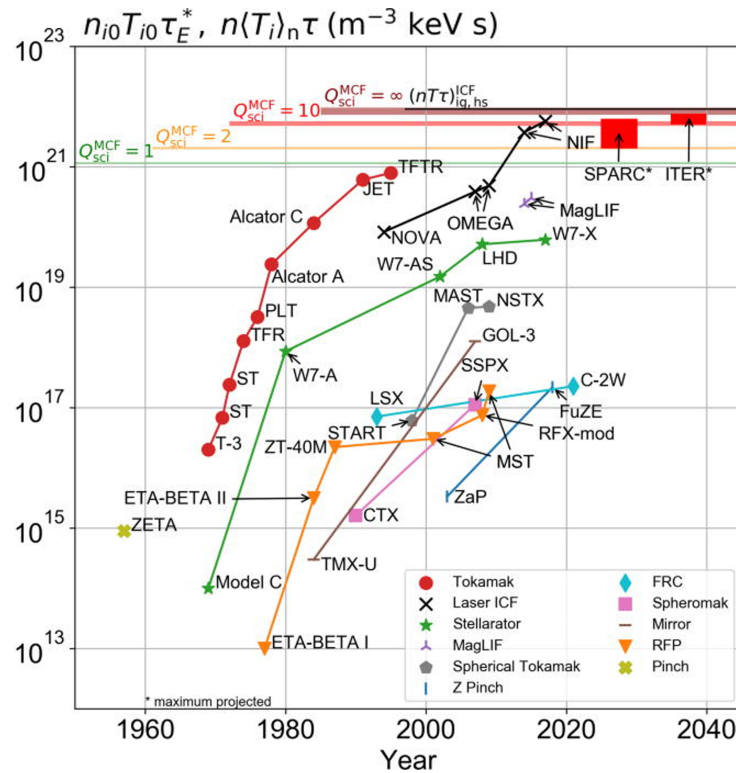


Figure 1: Progress of fusion research indicated by the triple product [13].

At the high temperatures of fusion experiments, particles enter the plasma state, the fourth fundamental state of matter. A plasma is an at least partially ionised gas consisting of freely moving ions (atomic nuclei) and electrons. These free charged particles cause plasmas to be electromagnetically conductive. To meet the criteria for nuclear fusion, the heated plasma must be confined, as it would immediately cool down if it interacted with its surroundings. The main types of confinement are gravitational confinement in extraterrestrial fusion processes, inertial confinement in laser-driven fusion experiments or military applications, and magnetic confinement, where the electromagnetic conductivity of the plasma is used to confine it using magnetic fields. In this thesis the focus is on magnetically confined plasmas.

2.2 Magnetic confinement

Magnetic confinement fusion exploits the behaviour of plasma particles in magnetic fields. These charged particles are directly affected by electric fields and, depending on their motion, by magnetic fields. The equation of motion of a charged particle with mass m , velocity \vec{u} and charge q in a magnetic field \vec{B} and an electric field \vec{E} reads [16]:

$$m \cdot \frac{d\vec{u}}{dt} = q \cdot (\vec{u} \times \vec{B} + \vec{E}) \quad (3)$$

This equation yields that moving particles in a magnetic field are forced on helical orbits perpendicular to the magnetic field. This circular motion is called gyration. In strong magnetic fields, the gyration radius becomes very small and the particle is therefore largely bound to the guiding centre of the motion, which follows the magnetic field lines [17]. While movement perpendicular to the magnetic field is strongly restricted, the particle can move freely parallel to the field. This property is used to confine plasmas in circular, closed magnetic fields. In plasma physics, this geometry is called a toroid, with the main directions being called toroidal and poloidal. Figure 2 shows a schematic of a toroid with the indicated directions.

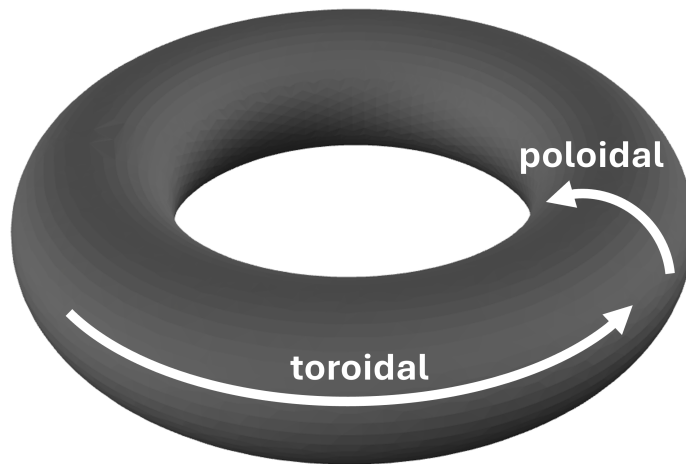


Figure 2: Schematic of a toroid [Own graphic].

However, a purely toroidal magnetic field, such as that of a ring-shaped solenoid, leads to a particle drift due to a stronger magnetic field on the inside of the torus. This drift ultimately leads to a loss of plasma confinement. In order to equalise this resulting particle drift and achieve equilibrium, helically twisted field lines are employed in magnetic fusion devices. A more in-depth description of this drift and

the necessity of a twisted magnetic field can be found in [12]. The twisted field lines lie on nested magnetic flux surfaces, which are characterised by being tangential to the magnetic field. The helical twist of the field depends on the flux surface r and is quantified by the rotational transform ι (iota). If the twisted field is interpreted as the superposition of a toroidal and a poloidal field component, ι can be defined as the change in the poloidal magnetic flux θ over the toroidal magnetic flux ϕ .

$$\iota(r) = 2 \cdot \pi \cdot \frac{d\theta}{d\phi} \quad (4)$$

If the rotational transform is an irrational value, a field line does not close on itself and eventually spreads out over the entire flux surface. A rational rotational transform implies that a magnetic field line is periodic after n poloidal turns (toroidal mode number) and m toroidal turns (poloidal mode number) [12]. It is then also given by

$$\iota(r) = \frac{n}{m} \quad (5)$$

The two main concepts for magnetic fusion devices are the tokamak and the stellarator. The difference between them is in the way they generate the rotational transform. In tokamaks the poloidal field component is created by inducing a toroidal current in the plasma itself. This current is generated by a solenoid at the centre of the tokamak, which carries a varying direct current. The main disadvantages of tokamaks are the inability to achieve steady-state operation and the susceptibility to current-driven instabilities, as the magnetic confinement depends on the plasma itself [18]. Figure 3a shows a simplified layout of a tokamak.

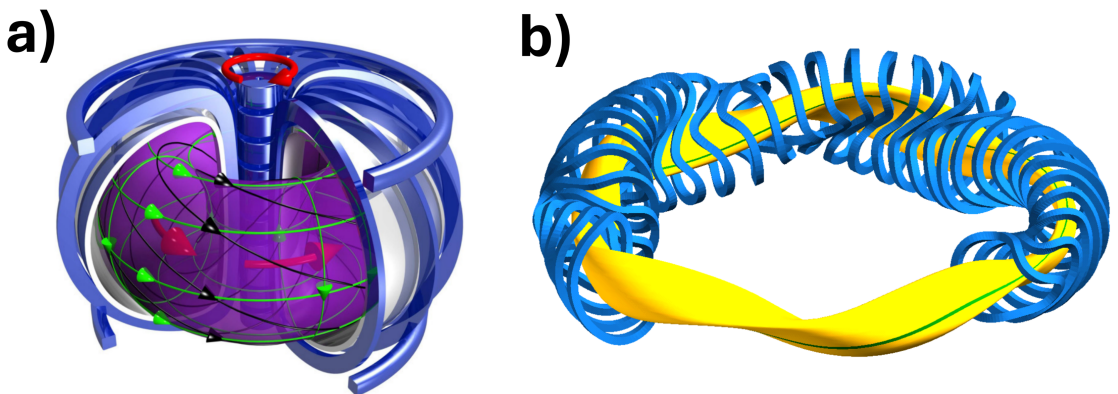


Figure 3: Tokamak (left) and stellarator (right) field coils and plasma configuration [Graphics: Max Planck Institute for Plasma Physics].

In stellarators the helically twisted field lines are generated solely by the field coils. There are several different types of stellarators, but they all share the characteristic that the plasma and coil configuration needs to be non-axisymmetric. The Wendelstein 7-X (W7-X) stellarator studied in this thesis is an optimised quasi-isodynamic stellarator. It creates its magnetic field by means of highly complex, non-planar field coils. Figure 3b shows the field coils (blue) and the plasma (yellow) of the W7-X, currently in operation at the Max Planck Institute for Plasma Physics in Greifswald, Germany.

Apart from achieving stable plasma confinement, the main function of a fusion reactor is to heat the reagents to the point of ignition. In magnetic confinement fusion, this is typically done by microwave radiation, neutral particle injection and/or Ohmic heating. After ignition, the fusion reaction given in formula 2 produces helium (alpha particles, when ionised) and very energetic neutrons. The charge of neutrons is zero and therefore they are not affected by the magnetic field. The neutrons leave the plasma and are stopped by the reactor wall, mainly on the so-called blanket. This blanket heats up and the heat can either be used directly or to generate electricity. The blanket is furthermore supposed to contain lithium, which interacts with the neutrons to produce tritium. This self-fuelling is necessary because tritium is a scarce element [5].

2.3 Divertor function and relevance

In magnetically confined plasmas, heat and particle transport occurs mostly parallel to the magnetic field. However, due to thermal conduction and diffusion processes, there is limited transport perpendicular to the field. This cross-field transport inevitably brings the plasma into contact with the reactor wall. In most magnetic fusion devices, the location of this plasma-wall interaction is determined by intentionally installed solid objects that intersect the flux surfaces. These objects are called plasma-facing components (PFCs). The primary function of the PFCs is particle exhaust and impurity retention, which is further described in Section 2.3.2. The PFCs separate the plasma into two regions: the main plasma with closed flux surfaces and the scrape-off layer (SOL) with intersected flux surfaces. At the boundary between the main plasma and the SOL is the separatrix. The last closed flux surface in the main plasma is referred to as the LCFS [19].

2.3.1 Plasma-wall interaction

The various processes that take place when a plasma interacts with a solid surface are the subject of study in the field of surface physics. At this point only the basic concepts are explained.

The most important surface interaction processes in fusion experiments are neutralisation, recycling and sputtering. The majority of the plasma particles that strike a surface will recombine on the surface and will be re-emitted as neutral particles. In the case of hydrogen, they can be re-emitted as atoms or molecules. It will be shown later that it is desirable to remove these neutrals by pumping them out of the plasma vessel. In W7-X this process is rather inefficient and therefore most of the neutralised particles interact with the plasma again. The high temperatures in the main plasma cause these particles to reionise. This process is called recycling, and the ratio of reionised plasma particles to the total number of plasma particles striking the surface is called the recycling coefficient \bar{R} [20].

The neutrals emitted can be further classified into three categories based on their energy. The intuitive process of simple reflection of the particle occurs with low probability. These back-scattered neutrals have an energy similar to that before recombination. Hydrogen atoms that originate from dissociated hydrogen molecules as a result of the Franck-Condon principle typically have an effective energy of 3 eV. A detailed description of this effect can be found in [16]. However, most of the incident particles are adsorbed on the surface thus "sticking" to the surface for a limited time. There they recombine into neutrals and are emitted as thermal particles with approximately the same thermal energy as the wall [12].

Sputtering occurs when energetic ions penetrate the surface and eventually eject solid particles from the surface. When the sputtered particles enter the main plasma as so-called impurities, the plasma interacts with them and cools down due to radiation losses. In general, impurities with higher atomic numbers (high-Z-impurities) lead to higher radiation losses. Sputtering also erodes the surface material over time. In advanced fusion experiments, the target material is often tungsten because of its low sputtering rate. Some devices also use carbon PFCs, as carbon impurities radiate less in a hot plasma [16].

2.3.2 Heat and particle exhaust

As explained in Section 2.3, the confined plasma inherently interacts with the reactor wall as a result of perpendicular transport. The PFCs in contact with the plasma edge are used for particle exhaust and impurity retention, which is essential for controlling plasma purity and density.

During a potential fusion reaction, alpha particles are produced which cause dilution of the core plasma, resulting in reduced collisionality between the fusing hydrogen ions. In addition, plasma impurities such as sputtered particles lead to radiation losses. In current fusion experiments, the concentration of impurities is a major limiting factor in energy confinement and must therefore be kept low. To combat the problems of helium dilution and impurity radiation, as many neutralised particles as possible are transported out of the plasma vessel, while at the same time fueling the plasma with new hydrogen [21].

While particle exhaust and impurity retention are necessary, the resulting energy exhaust on the PFCs is a drawback in fusion experiments. In strong magnetic fields, cross-field transport is severely limited, so the width of the SOL is typically very thin. As a result, the area of plasma-wall interaction is restricted to a very small region known as the wetted area. In non-neutron-producing fusion experiments, most of the energy exhaust is concentrated in this region, and therefore the PFCs have to cope with high heat fluxes. Modern PFCs are designed to withstand heat fluxes of $10 \frac{\text{MW}}{\text{m}^2}$ - $20 \frac{\text{MW}}{\text{m}^2}$ [22, 23, 24], similar to those found in rocket thrust chambers [25]. Research is focusing on how to increase the wetted area and thus reduce the heat flux. It is furthermore desirable to increase the energy losses of the plasma particles in the SOL before they strike the PFCs (e.g. by interacting with neutralised particles) [26].

The most straightforward concept for defining the plasma edge is the limiter, which defines the LCFS radially, as shown in Figure 4a on the next page. The main disadvantage of a limiter is that, due to its direct contact with the main plasma, the sputtered impurities interact almost immediately with the plasma, resulting in high radiation losses and limited energy confinement. In addition, the recycling coefficient in many limiter configurations is very high, which means that only a small fraction of the neutralised particles can be removed from the plasma vessel [5].

To overcome the problems of limiters, divertors have been developed which "divert" the location of the plasma-wall interaction away from the main plasma. The term "divertor" is used interchangeably for the required magnetic field configuration and the PFCs in that configuration. The development of divertors has led to higher plasma purities and recycling coefficients, and hence better energy confinement [16]. Figure 4b shows a scheme of a tokamak divertor configuration, known as a single-null divertor, with a characteristic null point in the separatrix called the X-point (X-loop in three dimensions). The field lines coming from the X-point are directed towards the targets. Field configurations with two X-points are called double-null divertors. Figure 4b also shows the pumping gaps in the plasma vessel which are intended to remove the neutralised particles. The space below the pumping gap is referred to as the sub-divertor region.

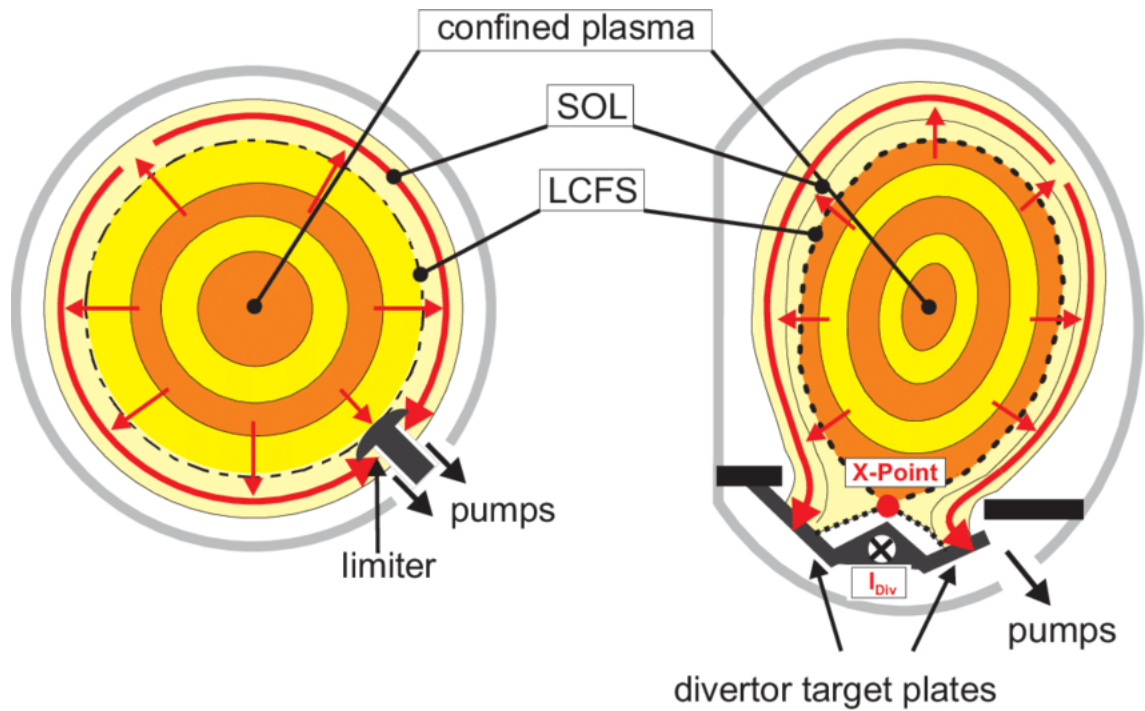


Figure 4: Limiter (left) and single-null divertor (right) configuration [27].

In the following, the basic properties of divertors are described analytically in formulae 6-11. This is done by modelling the LCFS as the particle and energy source and the divertor targets as the sink. The consequent pressure gradient along the SOL to the targets causes the transport processes in the SOL. Locations where the pressure gradient is zero are called stagnation points. The distance along a field line from the stagnation point to the divertor target is the connection length L_C , which

in tokamaks is given by the major plasma radius R and the rotational transform ι :

$$L_C \approx (2\pi)^2 \cdot \frac{R}{\iota} \quad (6)$$

It can be shown that the parallel velocity u_{\parallel} of the plasma particles in the SOL is typically equal to the ion sound speed c_s , which depends on the Boltzmann constant k_B , the electron temperature T_e , the ion temperature T_i and the ion mass m_i (the electron mass can be neglected).

$$u_{\parallel} = c_s = \sqrt{\frac{k_B \cdot (T_e + T_i)}{m_i}} \quad (7)$$

The combination of connection length and parallel velocity yields the typical particle dwell time in the SOL τ_{SOL} .

$$\tau_{\text{SOL}} \approx \frac{L_C}{c_s} \quad (8)$$

The radial width of the SOL λ_{SOL} is determined by the perpendicular velocity of the particles u_{\perp} .

$$\lambda_{\text{SOL}} \approx u_{\perp} \cdot \tau_{\text{SOL}} = u_{\perp} \cdot \frac{L_C}{c_s} \quad (9)$$

This perpendicular velocity is influenced by classical diffusion transport, neoclassical transport and turbulent transport. For simplicity, a diffusion coefficient D_{\perp} ($[D_{\perp}] = \frac{\text{m}^2}{\text{s}}$) merges these processes. u_{\perp} is then defined by:

$$u_{\perp} \approx \frac{D_{\perp}}{\lambda_{\text{SOL}}} \quad (10)$$

Inserting this definition of u_{\perp} into the formula for the radial SOL width results in the following equation [28]:

$$\begin{aligned} \lambda_{\text{SOL}} &\approx \frac{D_{\perp}}{\lambda_{\text{SOL}}} \cdot \frac{L_C}{c_s} \\ \Rightarrow \lambda_{\text{SOL}} &\approx \sqrt{\frac{D_{\perp} L_C}{c_s}} \end{aligned} \quad (11)$$

2.3.3 Plasma-neutrals interaction

In this section, three different scenarios for the interaction between the plasma particles in the SOL and the neutralised particles will be discussed.

Firstly, in the so-called sheath-limited regime it is assumed that the density in the SOL is low and therefore the plasma-neutrals interaction is negligible. In this case, the reionisation of neutrals only takes place at the LCFS and not in the SOL, which is why this regime is referred to as "low recycling". The absence of plasma-neutrals interaction leads to a simplified fluid model used to describe the plasma behaviour in the SOL. A fluid model is valid because the connection length is usually much longer than the mean free path between the plasma particles. The plasma fluid equations consist of particle, momentum, perpendicular and parallel energy conservation formulae. The simplified one-dimensional parallel energy conservation equations for ions (formula 13) and electrons (formula 14) are the sum of convective and conductive heat transport. In the formulae, q_{\parallel} is the parallel heat flux, x is the position on the linearised field line and κ is the specific thermal conductivity. Γ ($[\Gamma] = \frac{1}{\text{m}^2\text{s}}$) is the particle flux density and is calculated as the product of the particle density n ($[n] = \frac{1}{\text{m}^3}$) and the parallel velocity u_{\parallel} ($[u_{\parallel}] = \frac{\text{m}}{\text{s}}$) [28].

$$q_{\parallel} = q_{\parallel,\text{convection}} + q_{\parallel,\text{conduction}} \quad (12)$$

$$q_{\parallel,i} = \Gamma_i \cdot \left(\frac{1}{2} m_i u_i^2 + \frac{5}{2} k_B T_i \right) - \kappa_{0,i} T_i^{\frac{5}{2}} \frac{dT_i}{dx} \quad (13)$$

$$q_{\parallel,e} = \Gamma_e \cdot \left(\frac{5}{2} k_B T_e \right) - \kappa_{0,e} T_e^{\frac{5}{2}} \frac{dT_e}{dx} \quad (14)$$

In the low density scenario, it can be assumed that heat transport by conduction is minimal compared to convective transport. In this case there is no parallel temperature gradient in the SOL. As a consequence, the second part of the energy conservation equations is zero. With a constant $u_i = c_s$ the parallel heat flux scales linearly with the particle flux density. This property of the sheath-limited regime will be used in Section 4.6.

The second scenario is the so-called "high recycling", where higher densities in the SOL lead to higher collisionality between neutrals and plasma particles and subsequently to reionisation of the neutralised particles in the SOL. Due to the pressure gradient in the SOL, the reionised neutrals eventually strike the divertor

targets again and do not interact with the main plasma. This accumulation of particles leads to a lower pressure gradient in the SOL and therefore to a reduced convective heat transfer. Decreased convection and higher densities result in a temperature gradient in the SOL, causing conductive heat transfer. This is why this scenario is called conduction-limited regime [28].

At even higher densities in the SOL, the incident plasma particles lose enough energy through interaction with neutrals to recombine not on the divertor surface but in the volume in front of it. Since the plasma particles no longer impact on the surface, this case is referred to as detachment. Divertor detachment is advantageous for fusion experiments because the heat flux in the SOL is diffusely dispersed by radiation losses rather than concentrated in the small wetted area [26].

2.3.4 Island divertor concept

Axially symmetric X-loops, typically used in tokamak divertors, are not achievable in stellarators. Therefore, an alternative approach for stellarators is the island divertor concept, where topologically separate magnetic flux surfaces adjacent to the LCFS - the magnetic islands - are intersected by the divertor targets. Figure 5 shows the island divertor configuration of W7-AS (predecessor of W7-X [29]) in a poloidal cross section, with nine visible island cross sections encircling the main plasma.

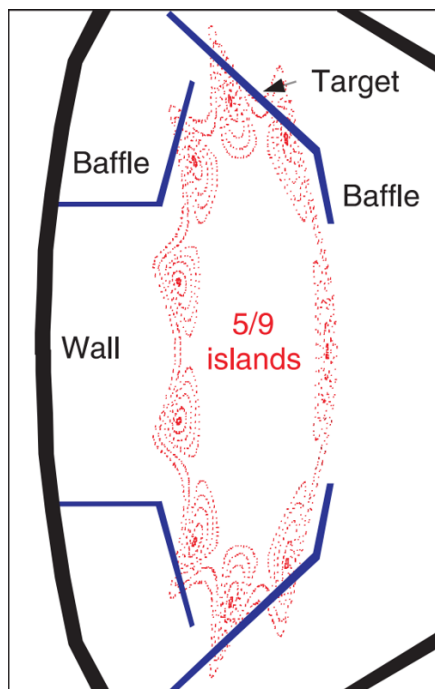


Figure 5: W7-AS island divertor configuration: the poloidal cross section shows nine island cross sections, six of which are intersected by divertor targets [30].

The basic idea of island divertors is the same as for tokamak divertors: due to perpendicular transport, particles from the main plasma diffuse into the island functioning as the SOL and interact with the divertor targets placed in the flux surfaces of the magnetic islands. In the W7-AS configuration of Figure 5, the targets intersect six of the nine present island cross sections. The term baffle refers to components adjacent to the divertor which are not in direct contact with the incident plasma particles. Nevertheless, they are exposed to heat radiation and are important for neutral particle transport. The size of the magnetic islands determines the distance from the plasma-wall interaction to the main plasma [19].

The existence of magnetic islands is closely related to the rotational transform explained in Section 2.2. Flux surfaces with a rational rotational transform $\iota = \frac{n}{m}$ are susceptible to radial magnetic field perturbations that "tear apart" a flux surface and form a magnetic island. The radial perturbation field can be applied either extrinsically by special coils or as an intrinsic feature of the magnetic field confining the plasma. The field perturbation needs to be spatially resonant with the flux surface dependent rotational transform [31]. In this case, the poloidal mode number of the perturbation determines the number of island cross sections. An example will illustrate this: a flux surface with $\iota = 1$ is resonant to $\frac{n}{m} = \frac{1}{1}; \frac{2}{2}; \frac{3}{3}; \dots$ radial perturbations and the resulting field exhibits 1; 2; 3; ... island cross sections. A flux surface with $\iota = \frac{5}{4} = 1.25$ is resonant to $\frac{n}{m} = \frac{5}{4}; \frac{10}{8}; \frac{15}{12}; \dots$ perturbations, which respectively lead to 4; 8; 12; ... island cross sections. The configuration of W7-AS in Figure 5 with $\iota = \frac{5}{9} = 0.\bar{5}$ is perturbed by a $\frac{n}{m} = \frac{5}{9}$ magnetic field and therefore shows nine island cross sections. Note that while the poloidal mode number determines the number of island cross sections, the integer multiple of the 1st harmonic of the field perturbation defines the number of magnetic islands. For example, a flux surface with $\iota = \frac{5}{4}$ perturbed by the 1st harmonic radial perturbation with $\frac{n}{m} = \frac{5}{4}$ will have only one magnetic island, which winds around the main plasma and closes on itself after four toroidal transits. In a poloidal cross section the same island is thus visible four times. The same flux surface perturbed by the 2nd harmonic radial perturbation with $\frac{n}{m} = \frac{10}{8}$ exhibits two magnetic islands and eight island cross sections [19]. A mathematical derivation of magnetic islands is described in [32].

2.4 Wendelstein 7-X

As of 2025, the W7-X fusion experiment is the world's largest stellarator and has been in operation since 2015 [33]. The main research objectives are to study steady-state high temperature plasmas in stellarator configurations and to demonstrate the reactor relevance of stellarators.

W7-X is a quasi-isodynamic stellarator utilising the **HELICAL Advanced Stellarator** (HELIAS) concept. The acronym constituent "Advanced" refers to a series of stellarators whose coil configurations have been optimised to achieve advantageous plasma confinement. The optimisation criteria of stellarators and in particular of W7-X, which has been optimised mainly with regard to neoclassical transport, are explained in [34] and [35]. This optimisation typically results in complex three-dimensional coil geometries, as seen above in Figure 3. The magnetic field is generated by 50 non-planar and 20 planar niobium-titanium superconducting coils cooled with liquid helium [36]. The term "helical" is misleading, as the first stellarator experiments were built with helical coils around the toroid to achieve the rotational transform. In contrast, W7-X consists of modular coils, allowing greater design flexibility and easier construction and maintenance. In W7-X, "helical" does not refer to the coil configuration, but to the helical path of W7-X's magnetic axis.

Figure 6 shows a cutaway diagram to illustrate the structure of W7-X. From inside to outside, it shows the plasma (pink), the plasma vessel, the non-planar (silver) and planar (orange) superconducting coils, the outer vessel and the helium pipes for cooling the coils. The space between the plasma vessel and the outer vessel still contains an ultra-high vacuum, which serves as thermal insulation for the cooled coils. Ports and domes provide access to the inside of the experiment. They contain vacuum pumps, diagnostics, heating systems or entrances for maintenance purposes.

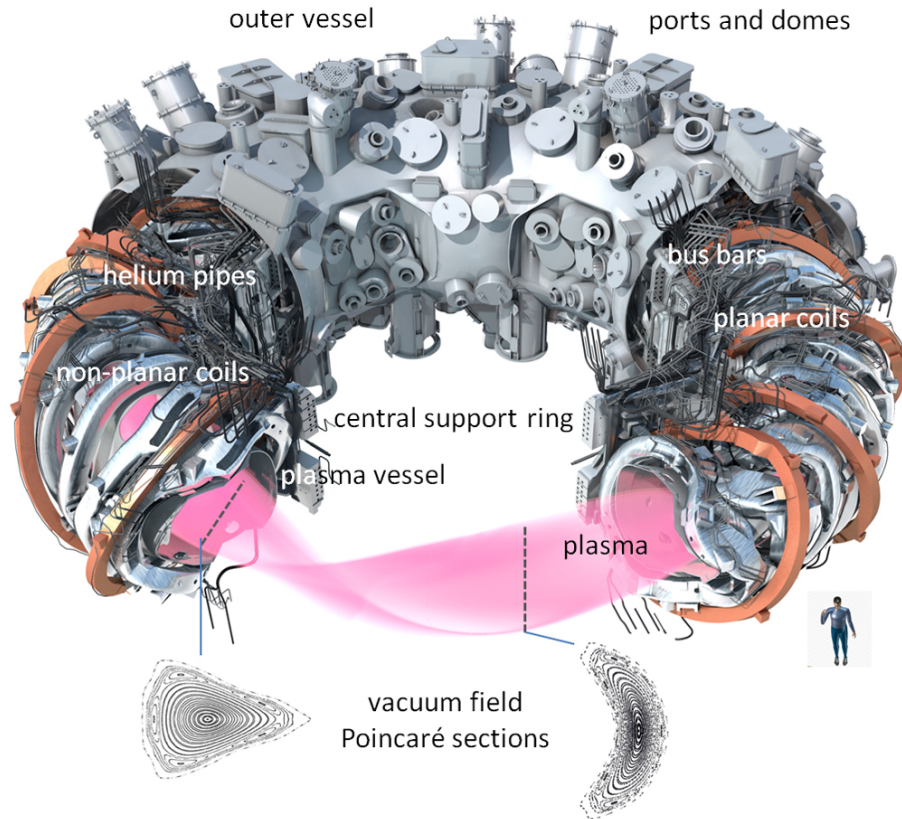


Figure 6: Cutaway diagram visualising the structure of W7-X; a sketched human serves as a size comparison [36].

W7-X is divided into five modules with identical coil and field configuration. Each of these modules consists of two mirrored half-modules, each with five non-planar coils and two planar coils. Figure 6 shows the magnetic field cross sections (Poincaré sections) at the beginning and end of a half-module. As shown, the geometry of the flux surfaces changes from "triangular" to "bean" shaped over the course of one half module [37].

2.4.1 Divertor configuration

When W7-X started operation in 2015, a limiter configuration with graphite PFCs was installed in order to carry out first experiments. To improve plasma performance, an uncooled carbon-fibre reinforced carbon (CFC) test divertor was deployed in 2017. This test divertor consists of ten identical divertor units intersecting the magnetic islands in the upper and lower plasma regions in each module of the fivefold symmetry [38]. Figure 7 shows the distribution of divertor targets around the LCFS.



Figure 7: Rendering of the divertor units (black) surrounding the LCFS (orange) [38].

Depending on the magnetic configuration, W7-X possesses a rotational transform and a corresponding harmonic perturbation field of $\iota = \frac{5}{5}$ (standard and high-mirror configuration), $\iota = \frac{5}{4}$ (high-iota configuration) or $\iota = \frac{5}{6}$ (low-iota configuration), resulting in 4, 5 or 6 visible magnetic islands [38]. In the $\iota = \frac{5}{5}$ configuration, five separate magnetic islands wind around the main plasma and close on themselves after one poloidal and one toroidal transit. The $\iota = \frac{5}{4}$ and $\iota = \frac{5}{6}$ configurations exhibit only one magnetic island, which closes after four respectively six toroidal transits. The test divertor has been designed to be suitable for all magnetic field configurations.

Figure 8 shows a blend of the as-built interior of W7-X with a flux surface cross section (green) in the standard configuration featuring five magnetic islands. The orange arrows indicate the perpendicular transport of plasma particles from the main plasma into the magnetic islands. The PFCs highlighted in red are the divertor targets, which intersect three of the five islands. The blue area is the wetted area, known as the strikeline, where the plasma particles strike the divertor targets and are neutralised.

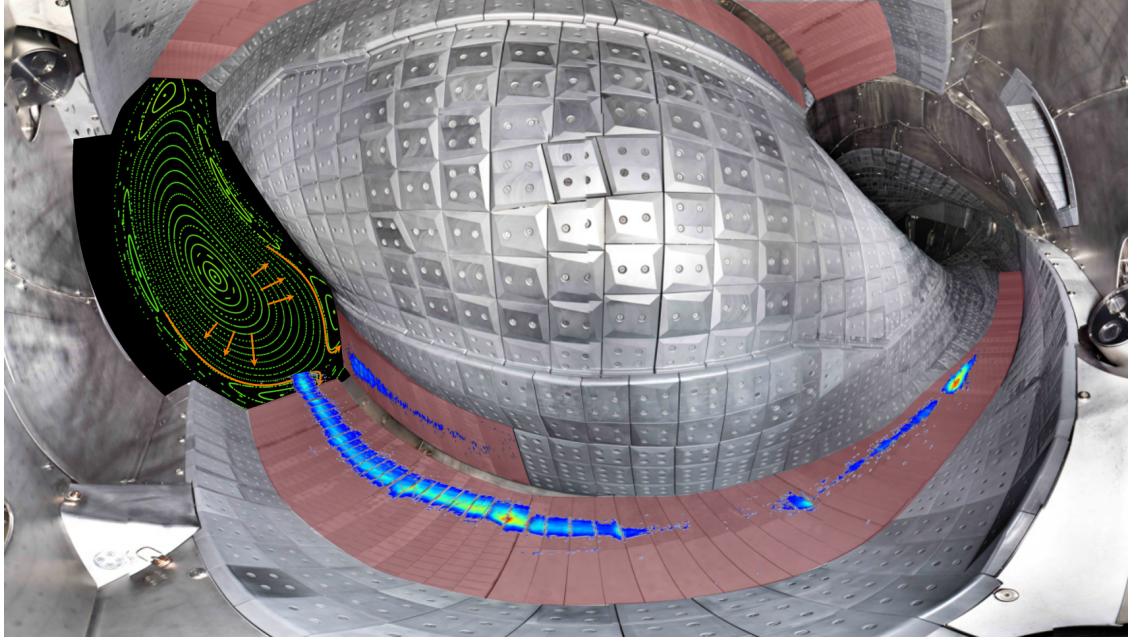


Figure 8: Image of the inside of the plasma vessel with the divertor targets highlighted in red, the strikeline (blue) and the magnetic flux surfaces (green) [Graphic: Daniel Böckenhoff, Max Planck Institute for Plasma Physics].

The CFC test divertor targets are designed to withstand heat fluxes of up to $10 \frac{MW}{m^2}$. To further improve steady-state performance, an actively water-cooled CFC divertor with CuCrZr heat sinks was installed in 2022 with identical geometry to the test divertor. These presently installed divertor targets are capable of handling stationary heat fluxes of $10 \frac{MW}{m^2}$ [22]. Research is currently underway on the planned future W7-X divertor, which will enter service after 2030. The targets will most likely be made of pure tungsten or a tungsten alloy with an actively cooled CuCrZr heat sink. A target geometry has not yet been selected [39].

2.4.2 Neutral particle transport

This subsection outlines the fundamentals and influencing factors of the neutral particle transport at W7-X simulated in the framework of this thesis. To expound the neutral particle transport, the geometry of a divertor unit is shown in Figure 9.

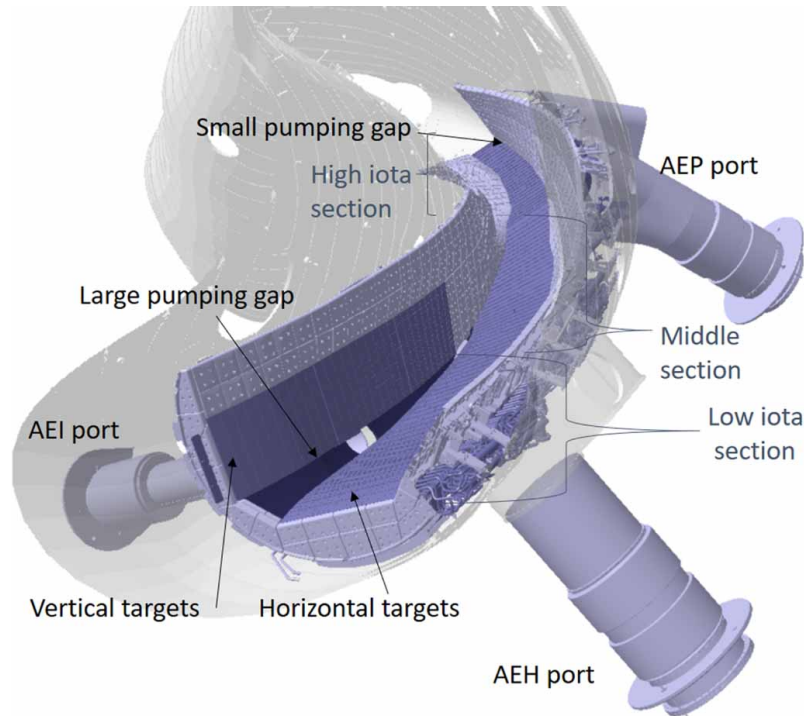


Figure 9: CAD rendering of one divertor unit showing the PFCs, the large and small pumping gaps and the ports connected to the sub-divertor [40].

Each of the ten identical divertor units consists of a low-iota, middle and high-iota section. The position of the strikeline, and therefore the position of the originating neutrals, changes according to the magnetic configuration. In the standard, high-mirror and low-iota configurations, the majority of particles are neutralised at the horizontal and vertical targets in the low-iota section, while in the high-iota configuration, the majority of particles strike the targets in the high-iota section. After their creation, the neutrals are intended to enter the sub-divertor region through either the large or small pumping gap. Closure plates separate the sub-divertor regions of the low-iota and high-iota sections. The AEH and AEP ports, connected to the sub-divertor region, contain turbomolecular vacuum pumps to remove the neutral particles from the plasma vessel. The effective pumping speed is $2350 \frac{1}{s}$ in the AEH port and $1180 \frac{1}{s}$ in the AEP port [40]. In W7-X, only a small fraction of the neutralised particles are pumped out of the plasma vessel. The remaining

neutrals can either interact with the surrounding walls or be recycled (reionised) in the confined main plasma or the SOL.

A single-reservoir particle balance, as described in [20], can be used to explicate the particle sources and sinks. In this context, the particle flux is denoted as γ ($[\gamma] = \frac{1}{s}$), in contrast to the particle flux density Γ ($[\Gamma] = \frac{1}{m^2s}$). The change in the total number of confined ions N_{tot} is the difference between the source and outflow particle fluxes. The outflow can be further described by the particle confinement time τ_p .

$$\frac{dN_{\text{tot}}}{dt} = \gamma_{\text{source}} - \gamma_{\text{outflow}} = \gamma_{\text{source}} - \frac{N_{\text{tot}}(t)}{\tau_p(t)} \quad (15)$$

There are four different particle sources in W7-X: the gas and pellet injection, the neutral beam injection (NBI) used to heat the plasma, and the recycling flow. The fuelling efficiency f determines the fraction of particles that actually reach the confined main plasma.

$$\gamma_{\text{source}} = f_{\text{gas}} \cdot \gamma_{\text{gas}} + f_{\text{pellet}} \cdot \gamma_{\text{pellet}} + f_{\text{NBI}} \cdot \gamma_{\text{NBI}} + f_{\text{recy}} \cdot \bar{R} \cdot \gamma_{\text{ion}}(t) \quad (16)$$

The last summand is important for the neutral particle transport. It describes the fraction of the total particle flux striking the divertor targets γ_{ion} that is reionised and reaches the main plasma. In a stationary case, γ_{ion} consists of the recycling particle flux γ_{recy} and the flux of particles pumped out of the plasma vessel γ_{pump} (the outflow). As mentioned in Section 2.3.1, the recycling coefficient \bar{R} is then given by the amount of recycled particles out of the total particle flux striking the targets. Experimental values yield a recycling coefficient of about 96 % - 98 % [20].

$$\gamma_{\text{ion}} = \gamma_{\text{recy}} + \gamma_{\text{pump}} \quad (17)$$

$$\bar{R} = \frac{\gamma_{\text{recy}}}{\gamma_{\text{ion}}} = \frac{\gamma_{\text{recy}}}{\gamma_{\text{recy}} + \gamma_{\text{pump}}} \quad (18)$$

When aiming for a constant N_{tot} , the external particle sources are bound to the pumped particle flux and vice versa. As γ_{pump} is small in the current divertor configuration at W7-X, this leads to limitations in the use of the NBI [41].

The neutral particle transport depends on a variety of factors. Section 4.1 discusses the extent to which the simulation performed takes these factors into account. In the first place, a number of plasma parameters determine the amount of particles entering the SOL, most importantly the plasma density [40]. The interplay of the magnetic configuration with the targets further defines the position and shape of the strikeline. The neutral gas density at the divertor targets dictates the plasma-neutrals interaction and whether the system is in the low-recycling, high-recycling, or detachment scenario. The geometry of the divertor targets and surrounding components determines the direction in which the neutrals are emitted. The transport of neutral particles in the sub-divertor region depends on the conductance of the sub-divertor structure (e.g. the ratio of the pumping gap area to the vacuum pump area), the neutral gas pressure in the sub-divertor with the associated flow regime (explained in 2.5.1) and the vacuum pump capacity and position.

2.5 Rarefied flow regimes

Rarefied flow regimes describe the behaviour of gases at very low densities, as for example in vacuum systems or high-velocity flows. In the following, the flow regimes are categorised according to the Knudsen number and it is shown that the neutral particle transport at W7-X is classified as a rarefied flow. Lambert’s cosine law is explained, which allows the quantification of surface scattering at low densities. In addition, the basic principle of the AC method is introduced, which is used by COMSOL for the calculation of rarefied flows.

2.5.1 Knudsen number

The Knudsen number Kn is used to determine the flow regime of the system. It is given by the ratio of the mean free path λ and the characteristic length l of the system.

$$Kn = \frac{\lambda}{l} \tag{19}$$

The mean free path is the average distance travelled by a particle before it collides with another particle. Assuming a Maxwell-Boltzmann distribution, the mean free path is given by the Boltzmann constant k_B , the temperature T , the particle diameter σ and the pressure p [42].

$$\lambda = \frac{k_B \cdot T}{\sqrt{2} \cdot \pi \cdot \sigma^2 \cdot p} \quad (20)$$

As the particle diameter is difficult to evaluate, the following simplified formula is commonly used, which includes the dynamic viscosity μ and the specific gas constant R_{specific} [43].

$$\lambda = \frac{\mu}{p} \cdot \sqrt{\frac{\pi \cdot R_{\text{specific}} \cdot T}{2}} \quad (21)$$

While the thresholds are not generally defined, four different flow regimes are typically distinguished. [44]:

- $\text{Kn} < 0.001$: Continuum flow
- $0.001 < \text{Kn} < 0.1$: Slip flow
- $0.1 < \text{Kn} < 10$: Transitional flow
- $\text{Kn} > 10$: Free molecular flow

Continuum flows, treated in classical fluid dynamics, are governed by particle collisions and can be described by the Navier-Stokes equations. Slip flows show a rarefied flow behaviour only in a thin layer adjacent to the system surfaces. In free molecular flows, the behaviour of gas is dominated by particle-surface collisions rather than inter-particle collisions. Consequently, particle trajectories can then be calculated unaffected by other particles. Transitional flows combine the properties of continuous and free molecular flows.

A rough calculation of the minimum Knudsen number at the large pumping gap in W7-X yields a value of $\text{Kn} = 1.94$, which classifies it as a transitional flow. The calculation is based on the pumping gap size $l = 90$ mm, the dynamic viscosity $\mu = 1.2 \cdot 10^{-5} \frac{\text{Pa}}{\text{s}}$ and the specific gas constant $R_{\text{specific}} = 4124.2 \frac{\text{J}}{\text{kg}\cdot\text{K}}$ [45]. Experimental values are used for the temperature $T = 200^\circ\text{C}$ and the pressure $p = 0.12$ Pa.

2.5.2 Lambert's cosine law

Lambert's cosine law quantifies diffusive processes and can be used to describe the angular distribution of particles emitted from a surface in free molecular flows. Irrespective of the incident angle, it states that the particle flux density Γ in a given direction is proportional to the cosine of the angle θ between that direction and the normal to the surface [43]. The maximum particle flux density $\Gamma(0)$ is found in the direction of the surface normal.

$$\Gamma(\theta) = \Gamma(0) \cdot \cos(\theta) \quad (22)$$

Figure 10 illustrates the cosine distribution of particles emitted from a surface. Note that in reality the emission process is much more complex [46].

The following is a two-dimensional calculation of the fraction of neutrals accessing the large pumping gap in W7-X using Lambert's cosine law. The values required are the diameter of the pumping gap d_{PG} and the distance from the pumping gap to the strikeline. Figure 10 shows the simplified model for the calculation with the horizontal and vertical divertor targets (bold lines) and the position of the strikeline (SL).

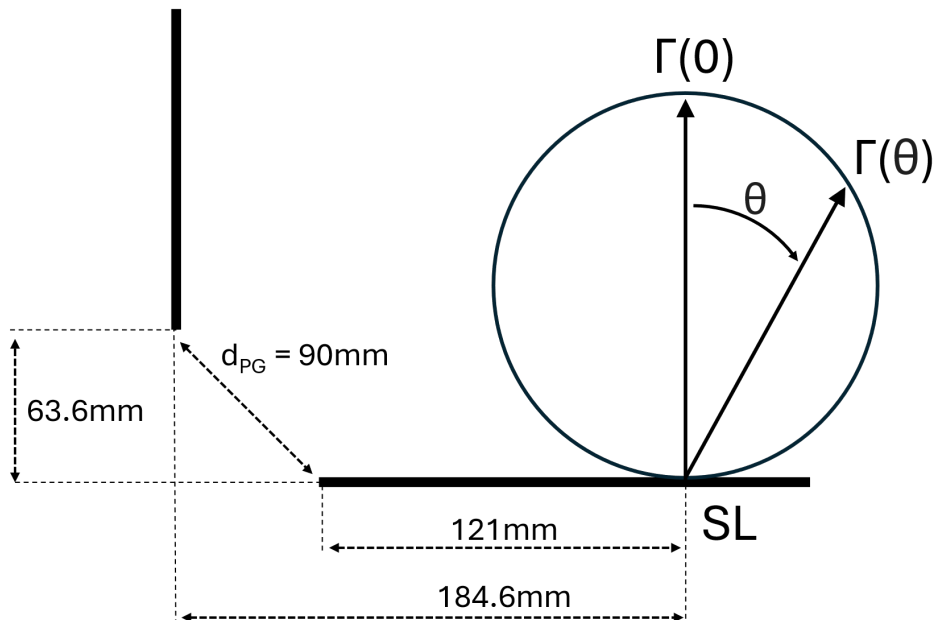


Figure 10: Scheme of the simplified two-dimensional calculation of particles entering the sub-divertor [Own graphic].

The opening angle α up to which the emitted particles enter the pumping gap can be determined geometrically.

$$\alpha = \arctan\left(\frac{63.6 \text{ mm}}{184.6 \text{ mm}}\right) = 0.33 \quad (23)$$

The particle flux fraction $d\gamma$ emitted by a line of length dL (dA in three dimensions) into an angular segment $d\theta$ ($d\Omega$ in three dimensions) is defined as

$$d\gamma = \Gamma(0)\cos(\theta)d\theta dL \quad (24)$$

Integrating this formula over the strikeline width L and the entire semicircle respectively the opening angle gives the total particle flux γ_{tot} and the particle flux entering the pumping gap γ_{PG} .

$$\gamma_{\text{tot}} = \int_0^L \int_{-\frac{\pi}{2}}^{\frac{\pi}{2}} \Gamma(0)\cos(\theta)d\theta dL = \Gamma(0)L \int_{-\frac{\pi}{2}}^{\frac{\pi}{2}} \cos(\theta)d\theta = 2\Gamma(0)L \quad (25)$$

$$\gamma_{\text{PG}} = \Gamma(0)L \int_{-\frac{\pi}{2}}^{-\frac{\pi}{2}+0.33} \cos(\theta)d\theta = \Gamma(0)L(\sin(-\frac{\pi}{2} + 0.33) - \sin(-\frac{\pi}{2})) = 0.054\Gamma(0)L \quad (26)$$

The ratio f of these values yields the percentage of particles entering the pumping gap. The low value of $f = 2.7 \%$ demonstrates the unfavourable neutral particle transport at W7-X due to the orientation of the divertor targets.

$$f = \frac{\gamma_{\text{PG}}}{\gamma_{\text{tot}}} = \frac{0.054\Gamma(0)L}{2\Gamma(0)L} = 2.7 \% \quad (27)$$

2.5.3 AC Method

While complex rarefied flows are often calculated using a Monte Carlo approach, COMSOL uses the Angular Coefficient (AC) method to compute rarefied flows deterministically and faster [47]. The AC method is based on the assumption that the incoming particle flux on a finite surface element is equal to the outgoing particle flux. The outgoing particle flux is described by a probability distribution function consisting of the Maxwell-Boltzmann distribution, used to represent the effect of surface temperature, and Lambert's cosine law. The incoming particle flux on a surface element is the sum of the particle flux fractions $d\gamma$ arriving from other surface

elements in the line of sight. COMSOL uses the hemicube method, typically used in computer graphics, to evaluate which surface elements are in the line of sight of the element under consideration. Figure 11 shows a strongly simplified visualisation of the AC method with three finite lines dL .

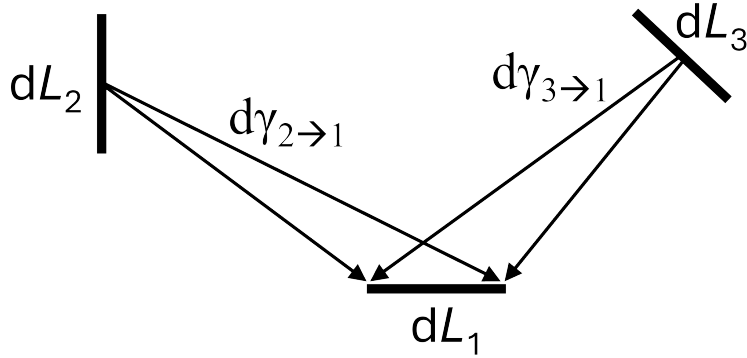


Figure 11: Simplified visualisation of the AC method [Own graphic].

There, the total incoming flux at dL_1 is the sum of the flux fractions arriving from the other finite lines $d\gamma_{2\rightarrow 1}$ and $d\gamma_{3\rightarrow 1}$. Defining the flux fraction $d\gamma_{n\rightarrow m}$ emitted by an element n and arriving at an element m as the product of the probability distribution $p_{n\rightarrow m}$ and the flux γ_n yields a linear system of equations (formulae 28 - 30) for the system in Figure 11. Further explanations and mathematical descriptions of the AC method can be found in [47] and [48].

$$\gamma_{1,\text{in}} = \gamma_{1,\text{out}} = p_{2\rightarrow 1} \cdot \gamma_2 + p_{3\rightarrow 1} \cdot \gamma_3 \quad (28)$$

$$\gamma_{2,\text{in}} = \gamma_{2,\text{out}} = p_{1\rightarrow 2} \cdot \gamma_1 + p_{3\rightarrow 2} \cdot \gamma_3 \quad (29)$$

$$\gamma_{3,\text{in}} = \gamma_{3,\text{out}} = p_{1\rightarrow 3} \cdot \gamma_1 + p_{2\rightarrow 3} \cdot \gamma_2 \quad (30)$$

3 Current transport codes and motivation

The high cost of fusion experiments makes prototyping infeasible. This underlines the importance of a simulation-first approach to refine designs before physical implementation. While in tokamaks it is often sufficient to model processes in two dimensions, the non-axisymmetric nature of stellarators requires three-dimensional simulations. The most sophisticated three-dimensional model currently used to simulate plasma edge and neutral particle transport in stellarators is the EMC3-Eirene code. EMC3 is used to stochastically solve the Braginskii plasma fluid equations, which consist of the mass, momentum, electron energy and ion energy conservation formulae [31]. In addition, EMC3 considers the interaction of plasma particles with impurities and neutralised particles by coupling EMC3 to the Eirene code. Eirene simulates the neutral gas dynamics according to the Boltzmann transport equation using a Direct Simulation Monte Carlo (DSMC) approach. EMC3-Eirene's capabilities include predicting heat deposition on the divertor targets, calculating the neutral fluxes at the PFCs and in the sub-divertor region, and computing the interaction of plasma particles with neutrals [49].

The downside of EMC3-Eirene is its inability to automatically generate meshes and its computationally intensive nature, requiring the use of high performance computers. Therefore, EMC3-Eirene is not suitable for fast iteration cycles of new divertor designs that need to be simulated with respect to thermal overload and neutral particle transport. EMC3-Lite was developed to address this problem. It allows the linear calculation of the heat deposition on the divertor targets, assuming a number of simplifications [50]. EMC3-Lite automatically creates meshes and solves the heat transport model in a few CPU minutes, allowing faster design iterations. The function of the divertor - the neutral particle exhaust - cannot be calculated by EMC3-Lite, as it is solely a plasma transport model.

In this thesis, a simplified simulation of the neutral fluxes at the divertor targets is presented. The model is coupled to EMC3-Lite and uses the AC method implemented in COMSOL to compute the neutral particle transport deterministically in a few CPU seconds to minutes. Until now, the neutral gas dynamics at divertor targets have not been calculated using a deterministic approach. However, there are previous deterministic simulations to evaluate the neutral particle transport in the sub-divertor

region. Haak et al. describe a simplified approach to model the neutral fluxes in the sub-divertor of W7-X using a heat radiation model in ANSYS. The model takes advantage of the fact that free molecular flows are calculated identically to photon dynamics [40]. Bi et al. simulated neutral particle transport in the sub-divertor of the planned China Fusion Engineering Test Reactor (CFETR) tokamak using the AC method in COMSOL. They showed that the AC method yields comparable results to Monte Carlo approaches [51].

The following section describes the simplifications made, the approach, the results, the validation and the improvement possibilities of the simplified neutral particle transport simulation performed.

4 Development of simplified neutral particle transport simulation

4.1 Deterministic approach

The aim of the simulation is to allow rapid comparison of new divertor designs in terms of neutral particle transport. The primary focus is on computational speed rather than on a highly comprehensive model of the actual physical processes. The main quantitative result of the simulation is the amount and ratio of particles entering the sub-divertor region, which is an important design criterion for the future W7-X divertor.

The starting point of the simulation is an employed code that converts the heat deposition on the targets calculated by EMC3-Lite into a neutral particle source in COMSOL. This conversion is described in Section 4.6. In order to allow a deterministic calculation of the consequent neutral gas dynamics, various simplifications had to be applied. In general, as the simulation is coupled to EMC3-Lite, all limitations of EMC3-Lite are also present in this simulation. In particular, this includes the restriction to low densities in the sheath-limited regime. It is therefore assumed that plasma-neutrals interaction in the SOL is negligible and that reionisation occurs only in the main plasma. Especially at higher densities, this approach leads to less accurate results. Furthermore, the simulation is limited to high Knudsen numbers and neglects inter-particle collisions. Section 4.10 discusses how to extend the simulation to transitional flows and how to consider reionisation in the SOL and divertor plugging. In addition, the COMSOL simulation does not account for radiative losses and is limited to a dual-species model (protium atoms and molecules). It is further assumed that all plasma particles interacting with the target surface are diffusely emitted as thermal neutrals.

4.2 Kisslinger file format

EMC3-Eirene and EMC3-Lite use the Kisslinger file format to represent geometry objects. The name originates from Johann Kißlinger, the physicist responsible for the design of the current W7-X divertor. Kisslinger files are simple quadrilateral mapped meshes with fixed poloidal and toroidal resolutions, suitable for easily describing surfaces in toroidal devices. Kisslinger meshes use polar coordinates consisting of the toroidal angle ϕ and the radial distance r with an additional z component. At a constant toroidal angle, the coordinate system can be interpreted as Cartesian. The quadrilateral mesh is constructed by dividing a surface into n_t toroidal cross-sections (cuts). Each toroidal cut contains a set of vertices that divide the surface into n_p poloidal cuts. The quadrilateral elements consist of four adjacent vertices. When working with Kisslinger files, it is usually advantageous to store the vertex coordinates not in lists but in three separate matrices of size (n_t, n_p) .

Figure 12 shows a schematic of a Kisslinger mesh consisting of $n_t = 5$ toroidal cuts and $n_p = 4$ poloidal cuts. The shown mesh consists of $(n_t - 1) \cdot (n_p - 1) = 12$ elements.

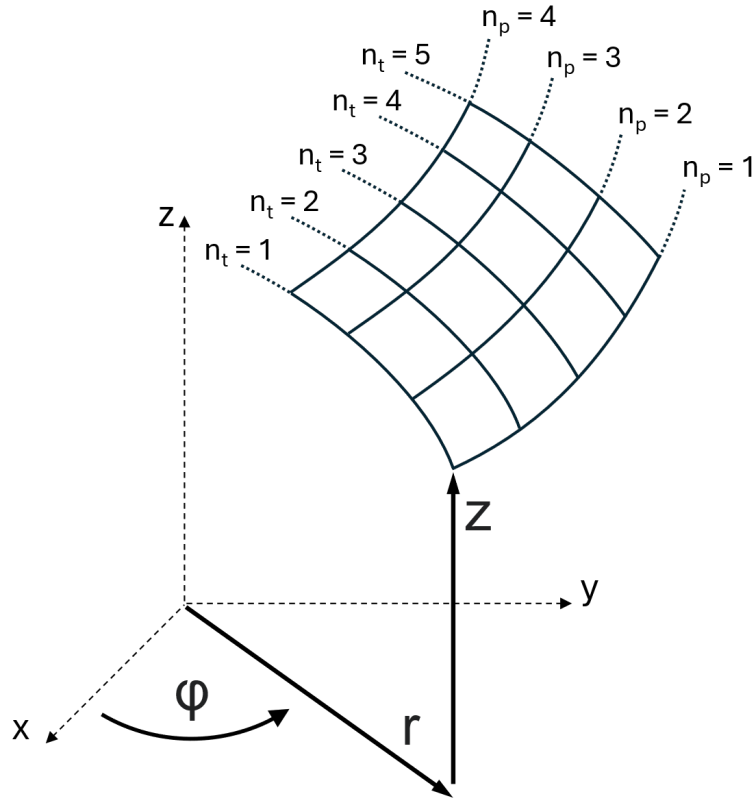


Figure 12: Schematic of a Kisslinger mesh of size $(n_t = 5, n_p = 4)$ with the specified coordinate system [Own graphic].

The main disadvantage of Kisslinger meshes is that they are not suitable for more complex structures. It is impossible to represent holes in the mesh or surfaces that divide into multiple parts. The fixed resolutions lead to uneven element sizes if there are size differences in the geometry.

As part of this thesis, several codes have been developed to convert Kisslinger files to other file formats. These include conversions to STL files, COMSOL native quadrilateral meshes (.mphtxt files) and point clouds. For simple geometries it has been possible to scale the Kisslinger meshes radially outwards from the magnetic axis. Combining this scaled Kisslinger mesh with the original mesh results in a voluminous hexahedral mesh, which can also be converted to a COMSOL native file.

4.3 Geometry

The geometry for the simulation is mainly taken from the Kisslinger meshes typically used for simulations performed with Eirene. These models are highly simplified and represent the considered divertor components, which consist of several parts, as surfaces. Due to the symmetry of W7-X, only 1/10 of the experiment is taken into account for the simulation.

In the simulated fraction of the experiment, the low-iota section of the divertor unit intersects the upper plasma region. Figure 13 shows the low-iota section in COMSOL with the horizontal and vertical divertor targets (blue), the left and right upper baffles (red) and a small part of the heat shield (yellow). The large pumping gap is closed by a cover (green).

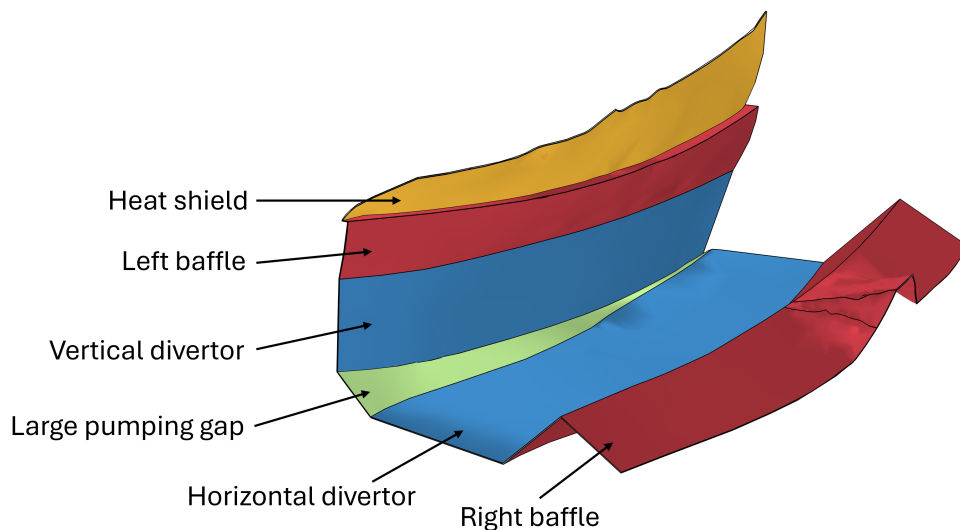


Figure 13: Coloured COMSOL rendering of the low-iota section [Own graphic].

The middle and high-iota sections of the divertor unit intersect the lower plasma region. The left image in Figure 14 shows these sections in COMSOL with the same colour scheme as above. The right image shows a close-up (view A) of the small pumping gap (green) at the end of the high iota section.

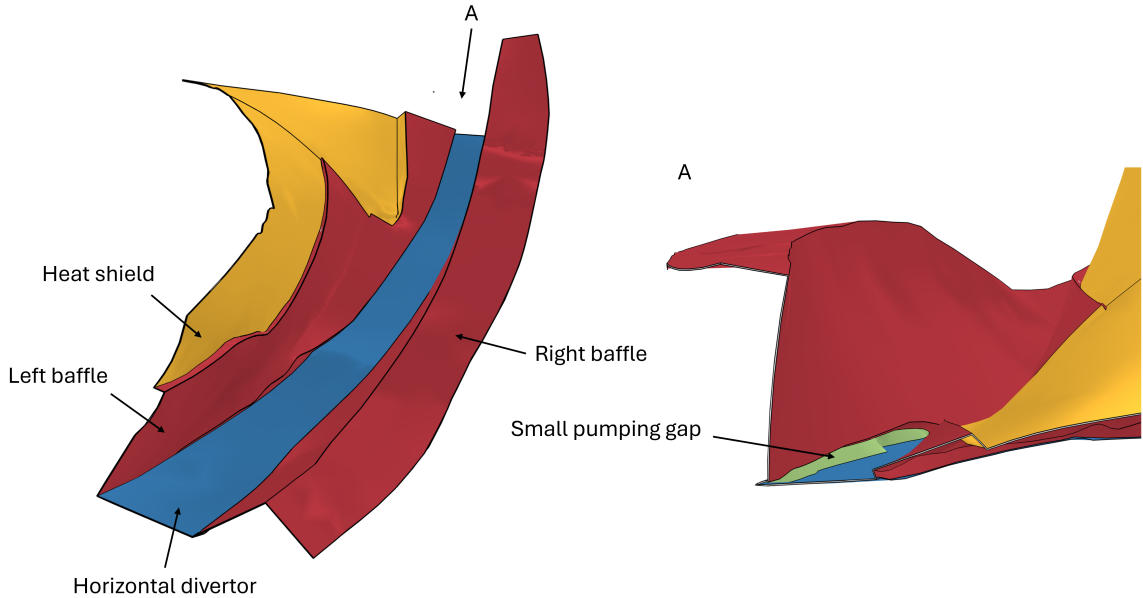


Figure 14: Coloured COMSOL rendering of the middle and high-iota sections [Own graphic].

The simulation further includes the LCFS, whose shape is determined by the magnetic configuration. Its geometry is given by a Fourier series computed by VMEC2000 (Variational Moments Equilibrium Code), which solves the basic magnetohydrodynamic force balance. This Fourier series is converted into a parametric surface in STEP format using the Python library CadQuery (code by Martin Banduch, Max Planck Institute for Plasma Physics).

For the AC method to converge, COMSOL requires a closed geometry. As the entire vacuum vessel of W7-X is too complex to be included in COMSOL, the system is artificially closed. This is done by subtracting the considered components from a larger torus. The result is a closed system with cavities in the shape of the simulated objects, as shown in Figure 15.

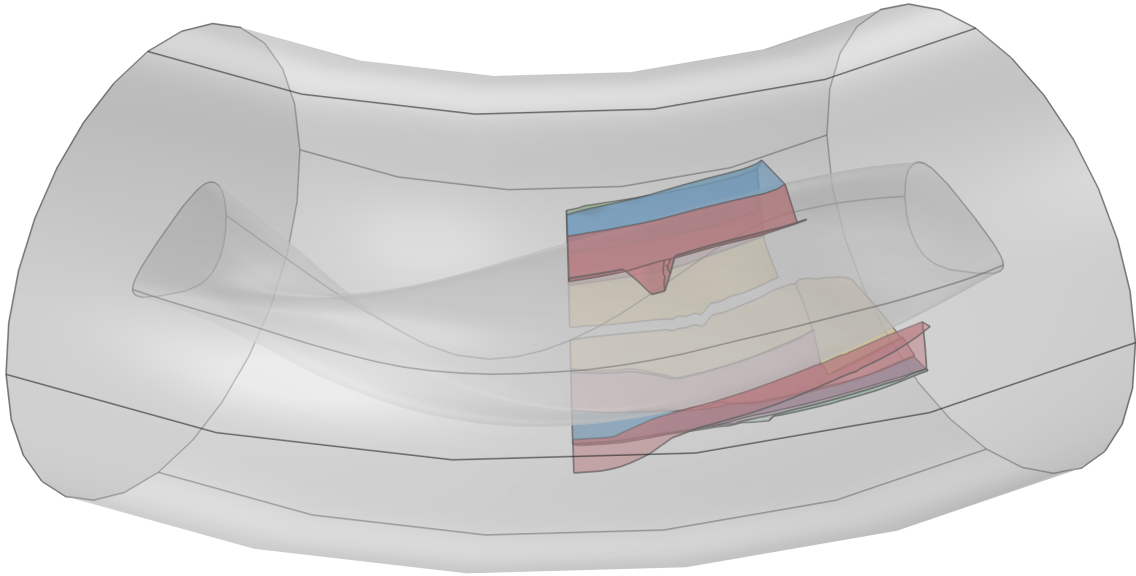


Figure 15: Transparent COMSOL rendering of the entire simulated geometry [Own graphic].

4.4 Meshing

The creation of a suitable mesh for the calculation of neutral particle transport turned out to be the most challenging task in the development of the simulation. The main approaches are outlined in this section. Most problems arose from the need to intersect the components with the larger torus, making a direct simulation on an imported mesh impossible. In addition, many Kisslinger files used for EMC3-Eirene simulations are partially deformed due to size differences in the geometry. Figure 16 shows a close-up of the Kisslinger mesh of the lower left baffle with deformed quadrilateral elements.

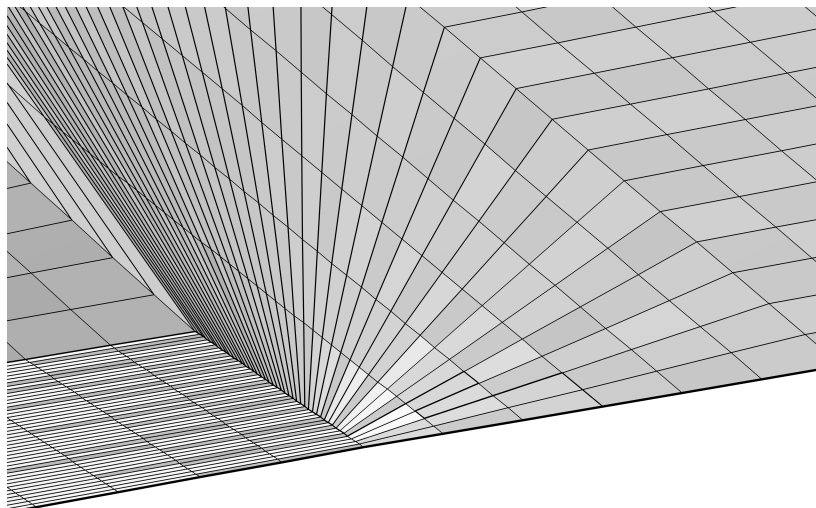


Figure 16: Deformations in Kisslinger files [Own graphic].

In the initial approach, the Kisslinger meshes were converted to STEP files by interpolating the toroidal cuts into surfaces using CadQuery. This resulted in geometric inaccuracies (waveforms) due to deformations in the Kisslinger files, as shown in Figure 17.

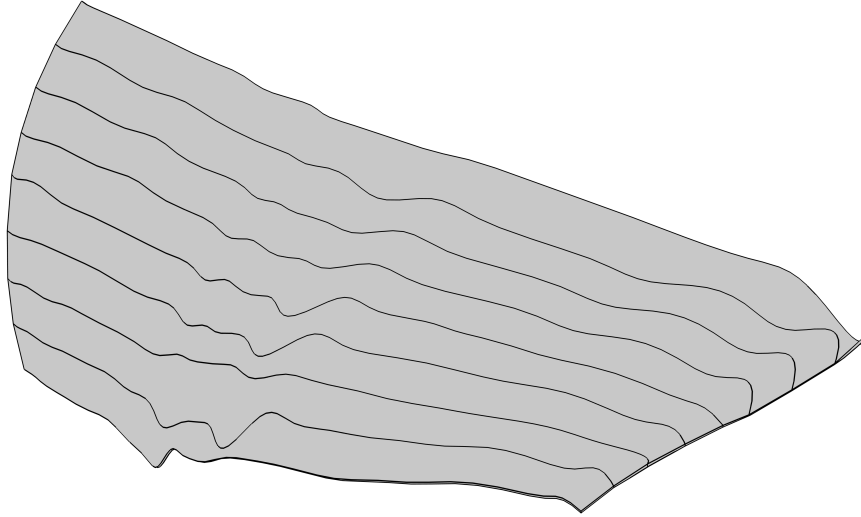


Figure 17: Waveforms in converted Kisslinger file [Own graphic].

In a subsequent approach, the Kisslinger files were directly imported into COMSOL where they were treated as native COMSOL geometry files. However, Boolean operations on the larger torus failed due to intersections within the Kisslinger files. These intersections of converted geometries are handled very inefficiently in COMSOL, resulting in unacceptable computation times.

In the final simulation, the components are combined directly as Kisslinger files. For this purpose, a code was developed that equalises the toroidal and poloidal resolution of two Kisslinger files by adding interpolated cuts to the existing meshes. This allows Kisslinger meshes to be easily merged. The code further calculates the intersection cut of two Kisslinger files and checks for duplicate cuts, which lead to errors when imported into COMSOL. This approach limits the simulation to non-intersecting and non-splitting geometries. Figure 18 shows the combined Kisslinger mesh of all the components that make up the simulated divertor unit.

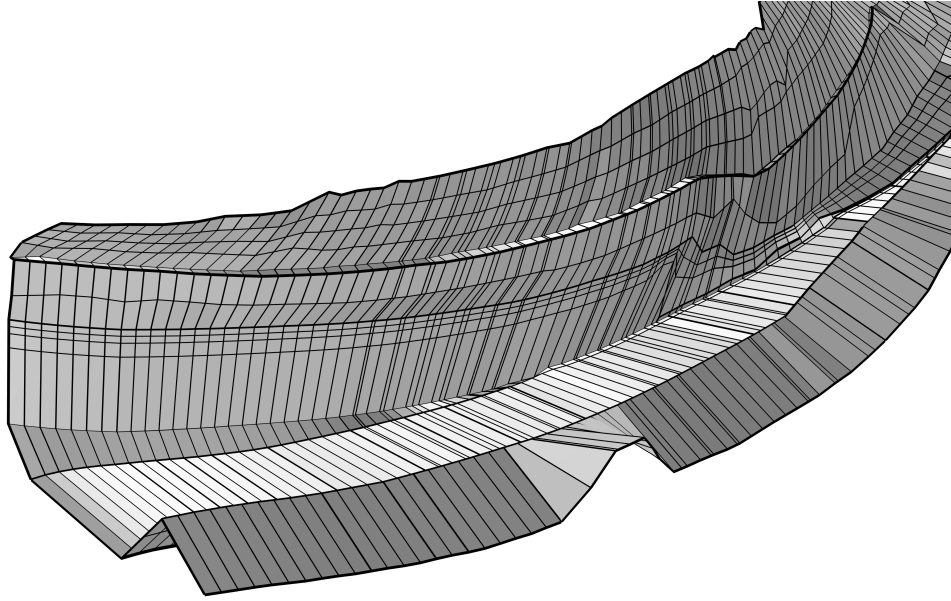


Figure 18: Combined Kisslinger mesh [Own graphic].

The combined Kisslinger meshes are then converted to COMSOL native meshes, imported into COMSOL, remeshed, thickened and converted to COMSOL native geometry files. The next step is to subtract these geometry files and the LCFS STEP file from the large torus. The final mesh is then generated by creating a triangular mesh on the boundaries of the resulting torus. Section 4.5 outlines the chosen element size. Figure 19 shows the final triangular mesh. Some boundaries of the large torus are hidden to allow a view on the simulated components.

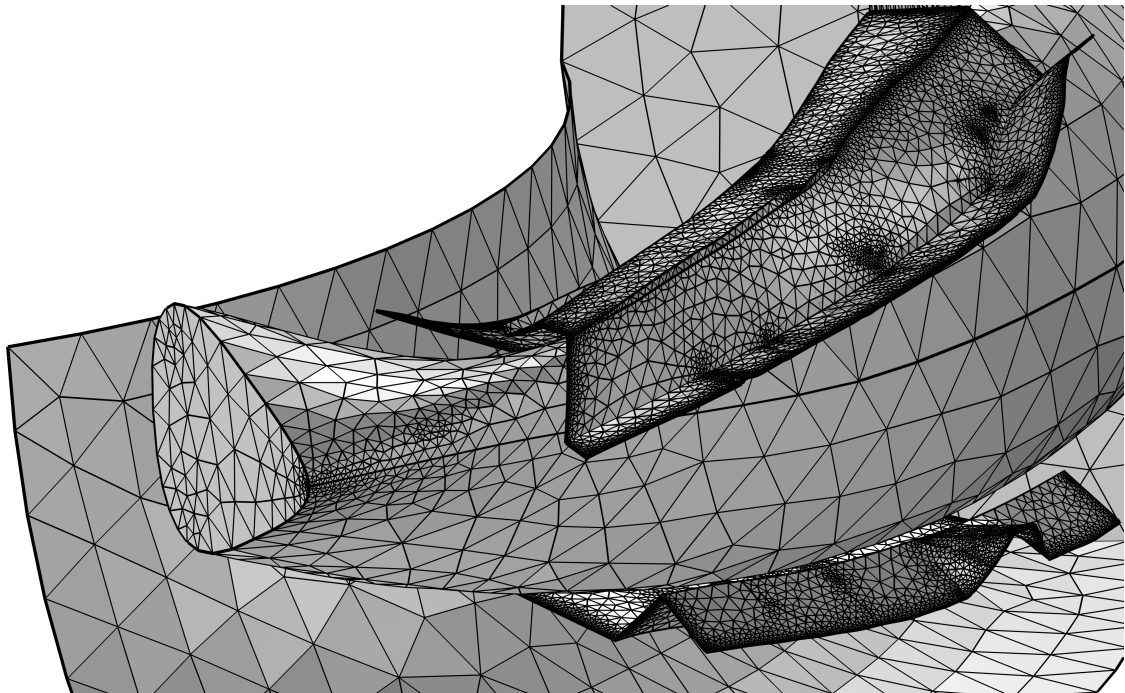


Figure 19: Final triangular mesh used in the simulation [Own graphic].

4.5 Resolution optimum

The following section explains the chosen element size applied to the triangular mesh shown in Figure 19. For this purpose, the simulation is performed with six different average element sizes A ranging from 3.15 cm^2 to 199 cm^2 . Predefined COMSOL parameters are selected for the different element sizes. The described element size refers only to the divertor components, as the mesh of the LCFS and the outer torus is generally coarser to save computing time. For each element size, the values of the particle fluxes to the large and small pumping gaps and the reionised particle flux are derived. The way these values are determined is described in chapter 4.8. Figure 20 shows the relative deviation of these values compared to those calculated with the finest mesh. Thus the relative deviation for the finest mesh with $A = 3.15 \text{ cm}^2$ is zero. Note that the relative deviation and the element size are scaled algorithmically. Figure 20 also shows the computing time of the simulation, which scales exponentially with smaller element sizes.

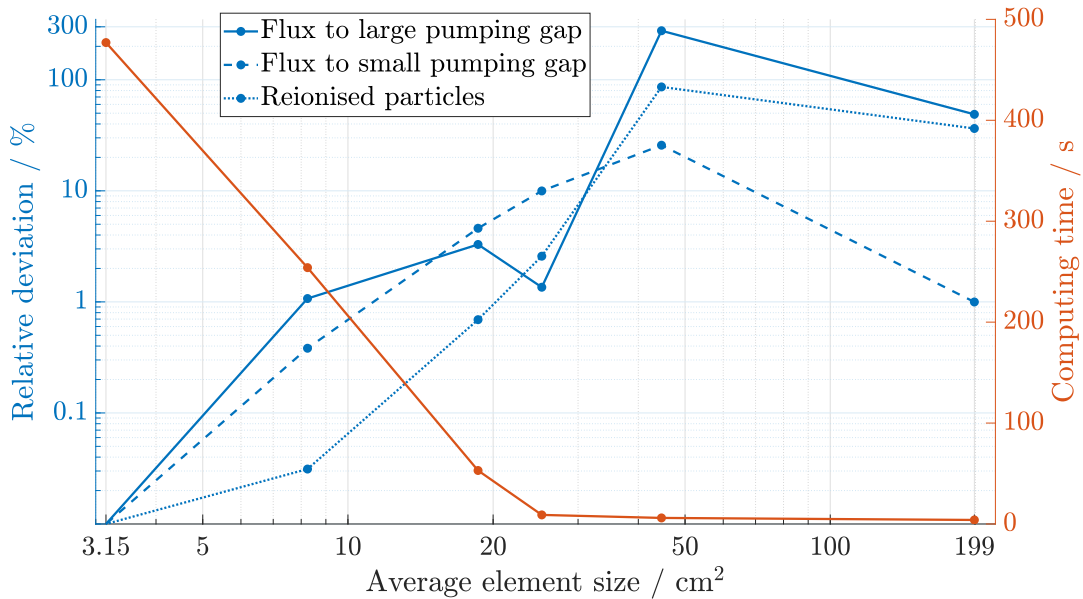


Figure 20: Relative deviation and computing time plotted against the average element size [Own graphic].

At the finest mesh, the automatic mesh generation fails and the maximum and minimum element size and curvature factor have to be manually adjusted. The finest mesh further results in high RAM usage of up to 40GB, making the simulation cumbersome to run. For this reason the second finest preset element size of $A = 8.25 \text{ cm}^2$ is chosen. The relative deviation for this element size is in an

acceptable range and does not significantly exceed 1 %.

In addition, the simulation was performed with different resolutions for the hemicube method, which had little effect on the results except for an exponential increase in computing time.

4.6 EMC3-Lite coupling

This section derives the conversion from the heat deposition data to the plasma particle flux distribution on the divertor targets. It further describes how this particle flux is interpreted as a neutral particle source in COMSOL.

EMC3-Lite calculates the heat deposition using a simplified Braginskii energy conservation formula, which consists of electron heat conduction parallel to the magnetic field and electron and ion heat conduction perpendicular to the magnetic field [50]. In this formula, $\kappa_e = \kappa_{e0} \cdot T^{\frac{5}{2}}$ is the Spitzer heat conductivity for electrons, n_e is the electron density, $T = T_e = T_i$ is the temperature and χ is the anomalous perpendicular heat conductivity.

$$\frac{\kappa_e}{n_e} \cdot \nabla_{\parallel}^2 \cdot T + \chi \cdot \nabla_{\perp}^2 \cdot T = 0 \quad (31)$$

In contrast to EMC3-Eirene, the right-hand side of the equation equals zero, as there are no energy sinks or sources due to plasma-neutrals interaction or impurity radiation.

The heat flux $q_{\parallel,t}$ at the targets is given by the Bohm sheath boundary condition (formula 32), which states that ions striking a wall are accelerated to at least the ion sound speed c_s [52]. ξ (usually γ in the literature) is the dimensionless sheath transmission factor, with a typical value for W7-X of 7.

$$q_{\parallel,t} = -\kappa_e \cdot \nabla_{\parallel} \cdot T = n \cdot c_s \cdot \xi \cdot T \quad (32)$$

The input parameters for EMC3-Lite are χ , n , T and the total power P_{SOL} in the SOL as well as the magnetic field and the target geometry. The parameters κ_{e0} , χ and ξ are constants. In the sheath-limited regime, the upstream and downstream temperatures are also constant. EMC3-Lite further assumes a constant density in the SOL. Consequently, there are no spatially dependent parameters in the formulae

31 and 32, so it can be assumed that the parallel heat flux scales linearly with the particle flux density Γ_t at the targets. Forming the quotient of these values with the total power in the SOL and the total particle flux γ_{SOL} in the SOL and setting them equal gives an expression for Γ_t .

$$\frac{q_{\parallel,t}}{P_{\text{SOL}}} = \frac{\Gamma_t}{\gamma_{\text{SOL}}}$$

$$\Gamma_t = \frac{q_{\parallel,t} \cdot \gamma_{\text{SOL}}}{P_{\text{SOL}}} \quad (33)$$

As the total particle flux in the SOL is difficult to evaluate, it is preferable to derive it from the EMC3-Lite input parameters. This is done by inserting $\Gamma_t = n \cdot c_s$ and the Bohm sheath boundary condition $q_{\parallel,t} = n \cdot c_s \cdot \xi \cdot T$.

$$n \cdot c_s = \frac{n \cdot c_s \cdot \xi \cdot T \cdot \gamma_{\text{SOL}}}{P_{\text{SOL}}}$$

$$\gamma_{\text{SOL}} = \frac{P_{\text{SOL}}}{\xi \cdot T} \quad (34)$$

With the EMC3-Lite default input parameters ($P_{\text{SOL}} = 1$ MW; $\xi = 7$; $T = 100$ eV), γ_{SOL} equals $8.92 \cdot 10^{21} \frac{1}{s}$. Inserting this term into formula 33 gives an expression for Γ_t that depends solely on the EMC3-Lite input parameters.

$$\Gamma_t = \frac{q_{\parallel,t}}{\xi \cdot T} \quad (35)$$

In equilibrium, all incident ions are emitted as neutral particles. For the CFC divertor targets and a protium plasma, this neutral flux is composed of about 90 % hydrogen molecules and 10 % hydrogen atoms. Therefore, a recombination factor of $f_{\text{recomb}} = 0.9 \cdot 0.5 + 0.1 = 0.55$ must be introduced. This defines the diffusely emitted neutral particle flux density Γ_{neutral} as:

$$\Gamma_{\text{neutral}} = \Gamma_t \cdot f_{\text{recomb}} = \frac{q_{\parallel,t} \cdot f_{\text{recomb}}}{\xi \cdot T} \quad (36)$$

EMC3-Lite evaluates this particle flux density for each quadrilateral element of the input Kisslinger meshes. In a first step, the data is stored at the vertices instead of at the elements by defining Γ_t at a vertex as the average particle flux density of the neighbouring Kisslinger elements. This particle flux density data at the vertices is

imported into COMSOL as simple tabular data. In COMSOL, this tabular data is interpreted as an interpolation function that describes the distribution of Γ_{neutral} as a scalar field. This function takes the coordinates x , y and z as input parameters, which must be multiplied by the reciprocal of their unit to obtain dimensionless input values. This interpolation function is subsequently used to define the outgoing particle flux at the target boundaries. Figure 21 shows a visualisation of the interpolated scalar field for the horizontal divertor in the low-iota section (left) and the imported neutral particle source in COMSOL for the standard configuration (right). The unit of measurement is $\frac{1}{\text{m}^2 \cdot \text{s}}$.

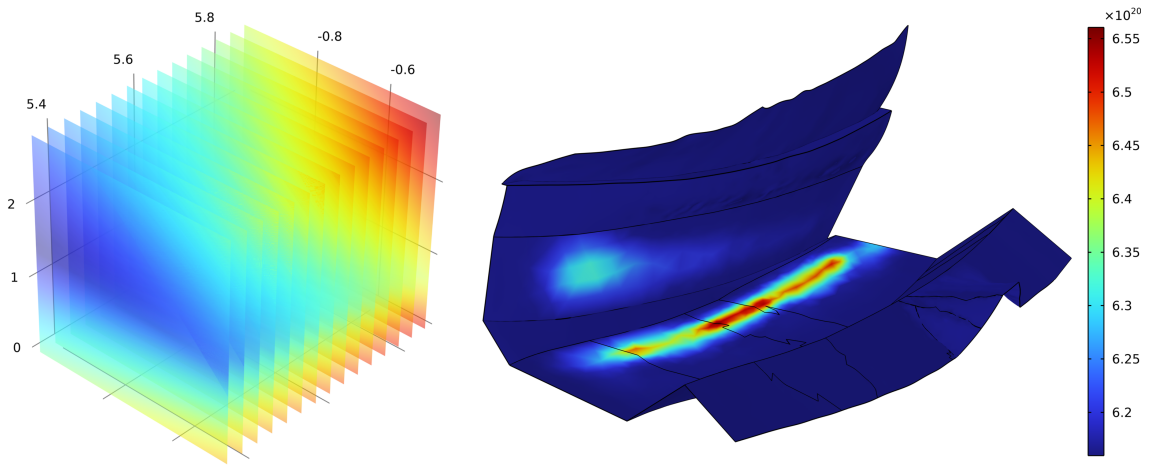


Figure 21: Interpolated flux density scalar field for the horizontal divertor in the low-iota section (left) and the neutral particle source in COMSOL for the standard configuration (right) [Own graphic].

4.7 Boundary conditions

The following section discusses the boundary conditions applied, with the exception of the neutral particle source on the divertor targets and baffles. Unless otherwise specified, the walls are assumed to be diffusely reflecting with a surface temperature of 200°C.

The surface temperature at the targets is derived from experimental values. Figure 22 shows the temperature distribution at the low-iota section of the divertor during an average discharge.

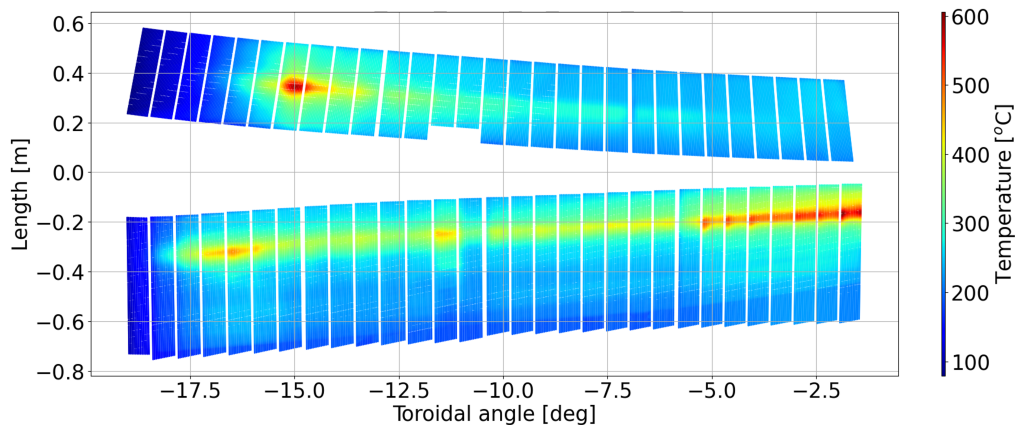


Figure 22: Temperature distribution on the divertor targets during an average discharge [Graphic: Yu Gao, Max Planck Institute for Plasma Physics].

Based on this distribution, it is estimated that at the location of the maximum incident particle flux density $\Gamma_{t,\max}$, the surface temperature is $T_t = 550^\circ\text{C}$. Assuming a linear correlation between the incident particle flux density and the surface temperature, the following equation is obtained.

$$T_t(\Gamma_t) = 350^\circ\text{C} \cdot \frac{\Gamma_t}{\Gamma_{t,\max}} + 200^\circ\text{C} \quad (37)$$

This formula is implemented in COMSOL in the same way as the interpolation function for the neutral particle source.

COMSOL additionally requires the molecular mass of the calculated species. The molecular mass of the neutral flux M_{flux} , consisting of 90 % hydrogen molecules and 10 % hydrogen atoms, is calculated with the molecular masses $M_{\text{H}_2} = 2.016 \frac{\text{g}}{\text{mol}}$ and $M_{\text{H}} = 1.008 \frac{\text{g}}{\text{mol}}$.

$$M_{\text{flux}} = 0.9 \cdot M_{\text{H}_2} + 0.1 \cdot M_{\text{H}} = 1.915 \frac{\text{g}}{\text{mol}} \quad (38)$$

The LCFS and the boundaries of the outer torus are defined as perfect particle sinks with an outgoing particle flux of zero at each finite element. The particle sink at the LCFS represents the reionisation of particles in the main plasma. The particles incidenting on the outer torus are the flux of particles leaving the divertor in poloidal or toroidal direction. In reality, most of these particles are also reionised after interacting with other W7-X components not included in the simulation.

The final boundary conditions are the particle sinks at the pumping gap covers. To account for the reentry of particles from the sub-divertor into the main chamber, only a fraction of the incidenting particles are removed at the pumping gap covers. The remaining particles are again emitted diffusely from the surface. The percentage of this particle outflux is taken from sub-divertor simulations performed with DIVGAS [53]. DIVGAS yields particle outflux percentages depending on the particle flux entering the sub-divertor of 72 % - 77 % for the large pumping gap and 38 % - 49 % for the small pumping gap. The COMSOL simulation uses average outflux percentages of $f_{\text{LPG}} = 74.5 \%$ for the large pumping gap and $f_{\text{SPG}} = 43.5 \%$ for the small pumping gap. It should be noted that these percentages will change when other divertor geometries are analysed.

4.8 Results

Under the specified boundary conditions, COMSOL solves for the incidenting particle flux density on each finite element using the PARDISO solver. In order to draw quantitative conclusions, the evaluated particle flux density is integrated over the considered boundaries. This surface integration yields the total particle flux γ on a surface. For example, the surface integral of the particle flux density at the LCFS represents the total flux of reionised particles. The surface integral is solved numerically as the sum of the total particle fluxes across the n_e finite elements that constitute the considered boundary.

$$\gamma = \int \int_S \Gamma \, dS \xrightarrow{\text{numerical}} \gamma = \sum_{i=1}^{n_e} A_i \cdot \Gamma_i \quad (39)$$

The neutral particle sources and sinks are subsequently compared to obtain a single-reservoir neutral particle balance for one divertor unit in equilibrium. The source of neutral particles is the neutralisation of incidenting ions at the PFCs, calculated by EMC3-Lite. EMC3-Lite furthermore calculates the leakage particle flux in the SOL γ_{leakage} , which are ions entering the SOL but not striking the targets, e.g. particles accumulating in the centre of the magnetic island (O-point). Particle sinks are the particle fluxes γ_{LPG} and γ_{SPG} entering the large respectively small pumping gap, the recycling flux γ_{recy} and the particles leaving the divertor in toroidal or poloidal direction $\gamma_{\text{tor/pol flux}}$.

$$f_{\text{recomb}} \cdot (\gamma_{\text{SOL}} - \gamma_{\text{leakage}}) = (1 - f_{\text{LPG}}) \cdot \gamma_{\text{LPG}} + (1 - f_{\text{SPG}}) \cdot \gamma_{\text{SPG}} + \gamma_{\text{recy}} + \gamma_{\text{tor/pol flux}}$$

$$f_{\text{recomb}} \cdot \left(\frac{P_{\text{SOL}}}{\xi \cdot T} - \gamma_{\text{leakage}} \right) = (1 - f_{\text{LPG}}) \cdot \gamma_{\text{LPG}} + (1 - f_{\text{SPG}}) \cdot \gamma_{\text{SPG}} + \gamma_{\text{recy}} + \gamma_{\text{tor/pol flux}} \quad (40)$$

The simulation was carried out for the standard, high-iota and high-mirror magnetic configurations. EMC3-Lite has been executed with the default parameters $P_{\text{SOL}} = 1$ MW, $\xi = 7$, $T = 100$ eV, $n = 10^{19} \frac{1}{\text{m}^3}$ and $\chi = 6 \frac{\text{m}^2}{\text{s}}$. In the following subsections, the results are visualised qualitatively and the particle sinks are quantified. Furthermore, the contribution of the different wall components to the neutral particle transport is discussed.

4.8.1 Standard configuration

In the standard configuration, the majority of neutrals originate at the horizontal divertor target in the low-iota section. Figure 23 shows this neutral source for the low-iota (left) and high-iota (right) sections. γ_{leakage} is 0.143 % of the total ion flux in the SOL.

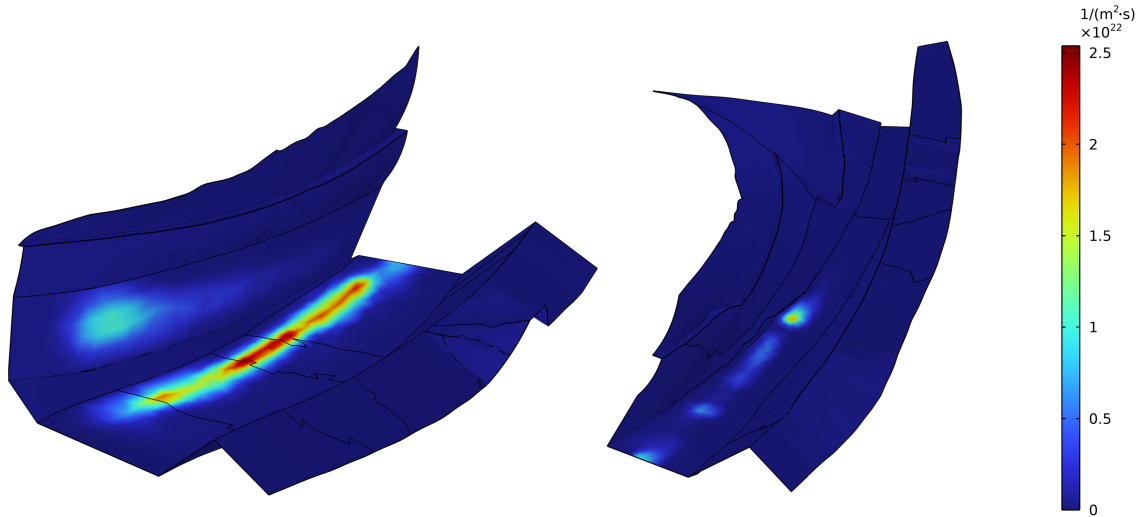


Figure 23: Neutral particle source for the standard configuration [Own graphic].

Figure 24 shows the simulated neutral particle flux density distribution in equilibrium. Logically, the highest flux densities are found at the vertical divertor target, which is closest to the strikeline. The figure shows that the majority of neutrals incident above the large pumping gap. In addition, only few neutrals reach the front of the divertor unit where the pumping gap has its largest diameter.

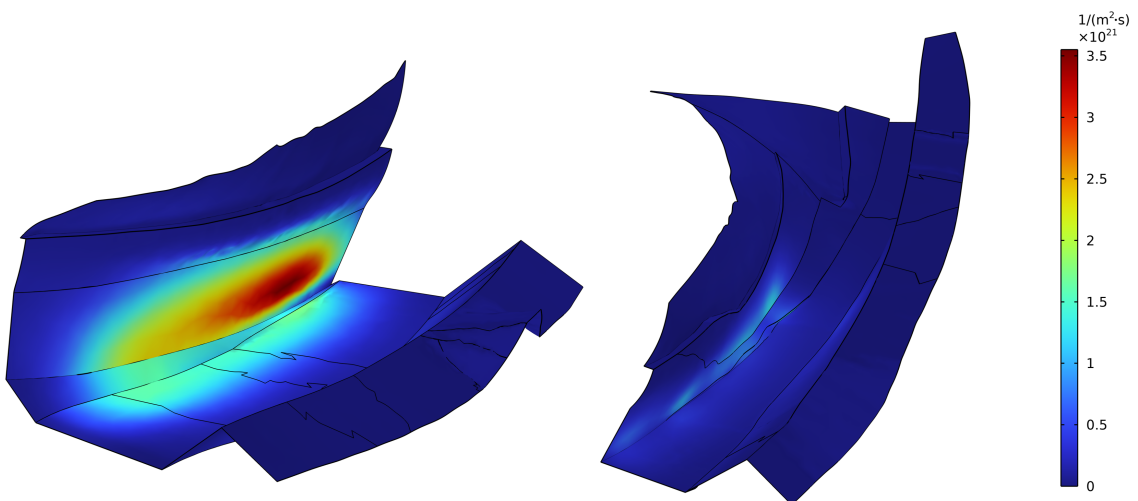


Figure 24: Calculated neutral particle flux distribution in the standard configuration [Own graphic].

Table 1 lists the absolute and relative values of the particle sinks explicated in formula 40. The relative values are determined in relation to the neutral source flux γ_{neutral} . The vast majority of particles are reionised in the main plasma, and only 2.73 % of neutrals reach the large pumping gap. Since very little neutrals are born in the high-iota section, the flux to the small pumping gap is negligible. Note that the percentages do not add up to 100 % because of the sub-divertor outflux.

Table 1: Calculated neutral particle sinks in the standard configuration.

	Particle flux / $10^{19} \frac{1}{s}$	Fraction of neutral source flux / %
γ_{LPG}	133.7	2.73
γ_{SPG}	3.5	0.07
γ_{recy}	4648.6	94.93
$\gamma_{\text{tor/pol flux}}$	212.3	4.34

Table 2 lists the total neutral particle fluxes at the wall components included in the simulation. The given fraction corresponds to the sum of particle fluxes to walls that do not act as particle sinks. Low/high-iota in brackets refers to the divertor section. The vertical and horizontal (low-iota) divertor targets and the left baffle in the low-iota section contribute predominantly to neutral particle transport. The heat shields play a minor role. This table does not include the incidenting ions at the divertor targets.

Table 2: Contribution of wall components to neutral particle transport in the standard configuration.

	Particle flux / $10^{19} \frac{1}{s}$	Fraction of total wall flux / %
Horizontal divertor (high-iota)	109.3	4.18
Horizontal divertor (low-iota)	579.7	22.17
Vertical divertor	1138.6	43.54
Left baffle (high-iota)	285.4	10.91
Right baffle (high-iota)	119.9	4.59
Left baffle (low-iota)	163.9	6.27
Right baffle (low-iota)	176.2	6.74
Heat shield (high-iota)	9.2	0.35
Heat shield (low-iota)	33.1	1.26

4.8.2 High-iota configuration

As the name suggests, in the high-iota configuration most neutrals originate in the high-iota section of the divertor. Figure 25 shows this source of neutral particles. γ_{leakage} is 0.291 % of the total particle flux in the SOL.

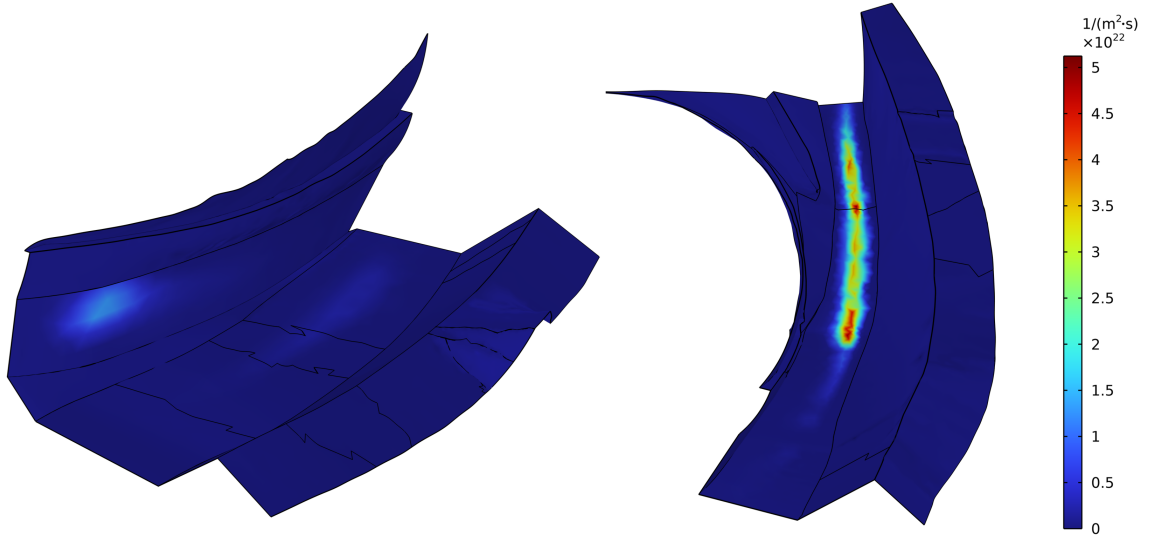


Figure 25: Neutral particle source for the high-iota configuration [Own graphic].

The neutral particle flux distribution in the high-iota configuration is shown in Figure 26. Again, the highest flux densities are found at the wall component closest to the strikeline, which in this case is the right baffle (high-iota). The low-iota section is almost uninvolved in the neutral particle transport.

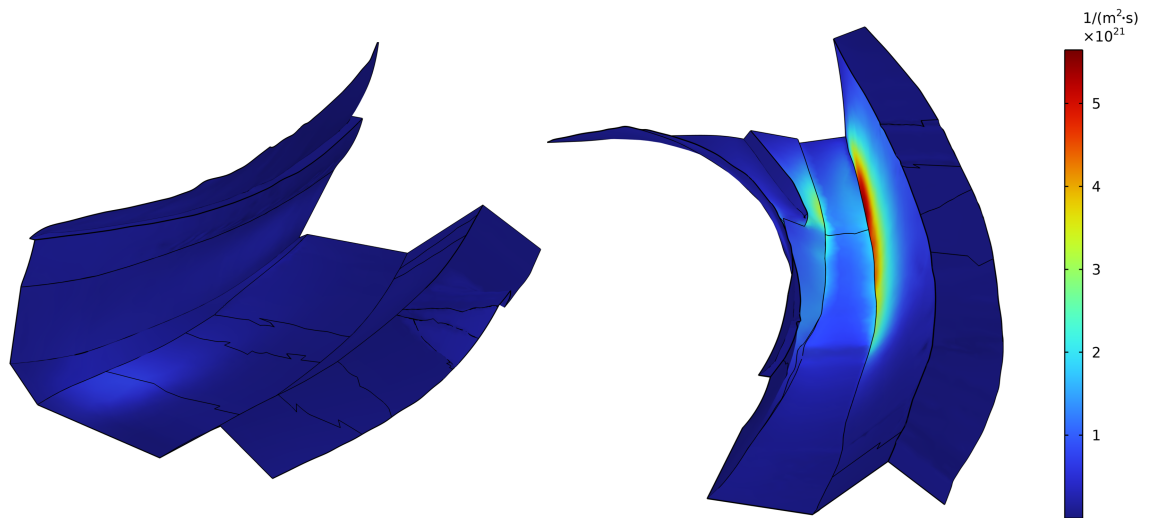


Figure 26: Calculated neutral particle flux distribution in the high-iota configuration [Own graphic].

The neutral particle sinks are listed in Table 3. As expected, the flux to the small pumping gap is much higher than γ_{LPG} . Furthermore, γ_{SPG} in the high-iota configuration is larger than γ_{LPG} in the standard configuration since the strikeline is closer to the pumping gap and the opening angle is partially larger. The reason for the high poloidal and toroidal flux is that the heat shield is "bent" inwards at the end of the high-iota section. This allows more particles to leave the divertor region in this direction.

Table 3: Calculated neutral particle sinks in the high-iota configuration.

	Particle flux / $10^{19} \frac{1}{s}$	Fraction of neutral source flux / %
γ_{LPG}	21.5	0.44
γ_{SPG}	139.6	2.85
γ_{recy}	3975.2	81.30
$\gamma_{\text{tor/pol flux}}$	830.2	16.98

The neutral particle fluxes to the wall components, listed in Table 4, show that the components in the high-iota section contribute primarily to the neutral particle transport. These are the left and right baffles and the horizontal divertor target.

Table 4: Contribution of wall components to neutral particle transport in the high-iota configuration.

	Particle flux / $10^{19} \frac{1}{s}$	Fraction of total wall flux / %
Horizontal divertor (high-iota)	530.3	16.31
Horizontal divertor (low-iota)	127.3	3.92
Vertical divertor	79.5	2.45
Left baffle (high-iota)	967.8	29.77
Right baffle (high-iota)	1349.4	41.51
Left baffle (low-iota)	20.3	0.63
Right baffle (low-iota)	38.4	1.18
Heat shield (high-iota)	117.6	3.62
Heat shield (low-iota)	20.0	0.62

4.8.3 High-mirror configuration

In the high-mirror configuration, the largest neutral particle source is at the vertical divertor target. In addition, there is a smaller strikeline at the horizontal divertor in the low-iota section. The neutral particle source for this configuration is shown in Figure 27. γ_{leakage} is 0.064 % of the total ion flux in the SOL.

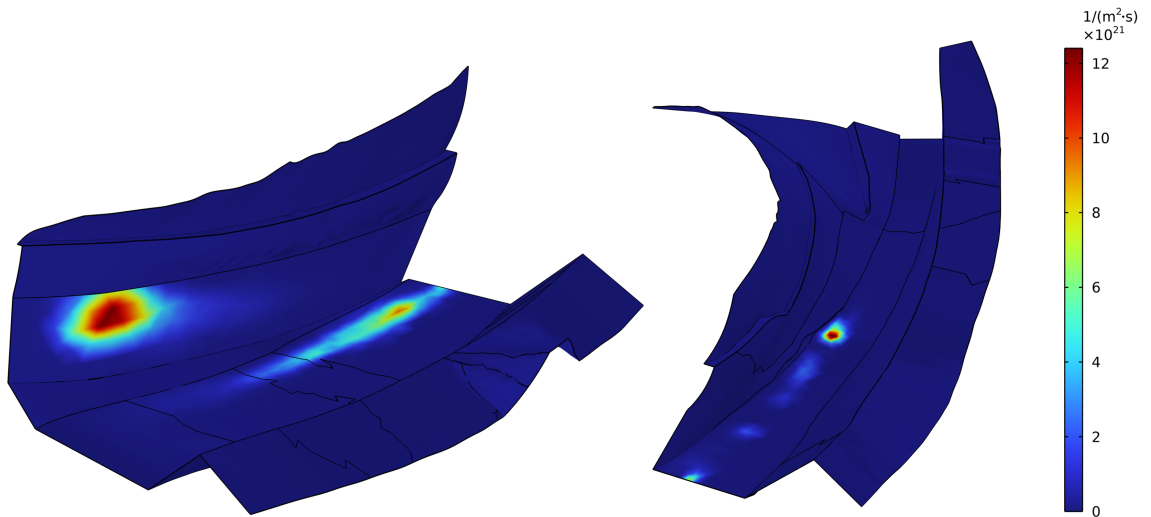


Figure 27: Neutral particle source for the high-mirror configuration [Own graphic].

Figure 28 shows the resulting neutral particle flux distribution in the high-mirror configuration. The highest flux densities are found at the vertical divertor, close to the smaller strikeline. The neutral source at the vertical divertor is located too far away from the large pumping gap and the horizontal target, causing many particles to be directly reionised.

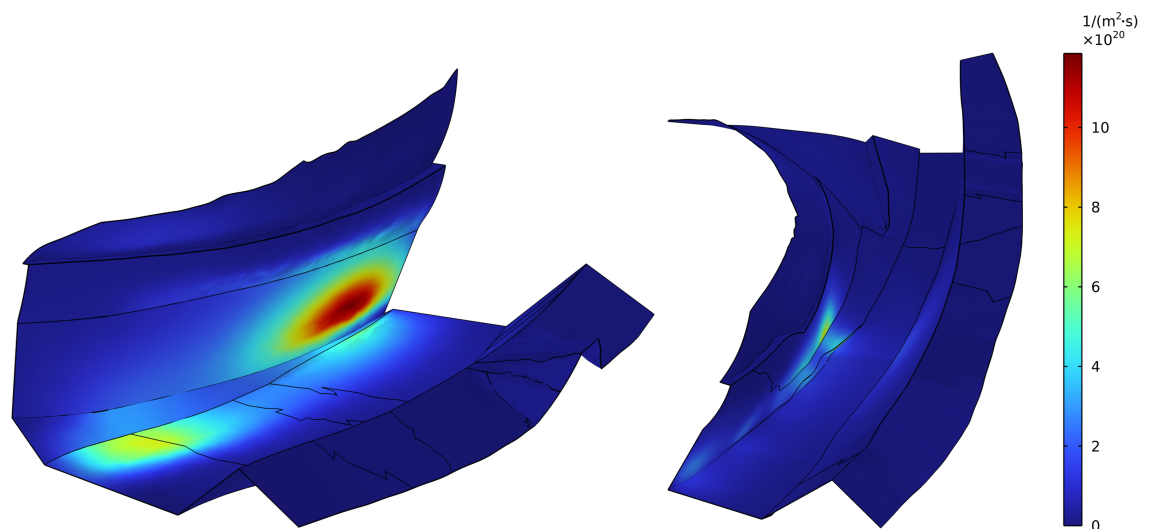


Figure 28: Calculated neutral particle flux distribution in the high-mirror configuration. [Own graphic].

The quantified particle sinks, listed in Table 5, are similar to those in the standard configuration. Since the main neutral particle source is further away from the large pumping gap, γ_{LPG} is 0.66 % less than in the standard configuration.

Table 5: Calculated neutral particle sinks in the high-mirror configuration.

	Particle flux / $10^{19} \frac{1}{s}$	Fraction of neutral source flux / %
γ_{LPG}	101.6	2.07
γ_{SPG}	4.7	0.10
γ_{recy}	4636.3	94.60
$\gamma_{\text{tor/pol flux}}$	236.0	4.82

Table 6 summarises the contribution of the wall components to neutral particle transport in the high-mirror configuration. As in the standard configuration, the highest fluxes are found at the horizontal and vertical divertor targets and the left baffle in the low-iota section.

Table 6: Contribution of wall components to neutral particle transport in the high-mirror configuration.

	Particle flux / $10^{19} \frac{1}{s}$	Fraction of total wall flux / %
Horizontal divertor (high-iota)	117.7	5.33
Horizontal divertor (low-iota)	574.0	25.98
Vertical divertor	727.2	32.92
Left baffle (high-iota)	320.0	14.49
Right baffle (high-iota)	140.2	6.34
Left baffle (low-iota)	150.6	6.81
Right baffle (low-iota)	98.5	4.46
Heat shield (high-iota)	17.0	0.77
Heat shield (low-iota)	64.0	2.90

4.9 Validation

This section discusses the accuracy of the derived values. A comprehensive validation of the simplified neutral particle transport simulation is left for future work.

The general correctness of the simulation is demonstrated by the good agreement with the analytical calculation in Section 2.5.2. This calculation yields a value for $\frac{\gamma_{\text{LPG}}}{\gamma_{\text{neutral}}}$ of 2.7 % and the simulation yields $\frac{\gamma_{\text{LPG}}}{\gamma_{\text{neutral}}} = 2.73$ % (standard configuration).

This proportion of neutralised particles entering the sub-divertor region has not been extensively investigated experimentally. A first approach is described by Wenzel et al. [54], who evaluated this ratio for a single discharge in the standard configuration. In this paper $\frac{\gamma_{\text{LPG}}}{\gamma_{\text{neutral}}}$ is referred to as PCE (particle collection efficiency). γ_{neutral} is derived from measurements of visible light cameras with narrow band pass filters for H_α [55]. γ_{LPG} is obtained from measurements of the neutral gas pressure gauge at the large pumping gap [56]. γ_{SPG} cannot be determined because there is no neutral gas pressure gauge at the small pumping gap. The considered discharge (20180905.30) is characterised by a line-integrated density of $11 \cdot 10^{19} \frac{1}{\text{m}^2}$, a heating power of 6 MW and a radiated power fraction of 47 %. For this discharge, Wenzel et al. calculated a value for $\frac{\gamma_{\text{LPG}}}{\gamma_{\text{neutral}}}$ of 0.69 % \pm 0.28 %. Therefore, the value calculated by COMSOL is about a factor of 4 larger than this experimental value. The effect of different plasma parameters remains unclear.

Boeyaert et al. [41] simulated the neutral particle transport with EMC3-Eirene. Figure 29 shows the results for the neutral particle fluxes at 3 MW and 5 MW input power as a function of the line-integrated density. The calculated fraction of particles entering the sub-divertor ranges from 4.0 % to 10.4 %. So far, the neutral particle transport simulation with EMC3-Eirene has only been performed for the standard configuration.

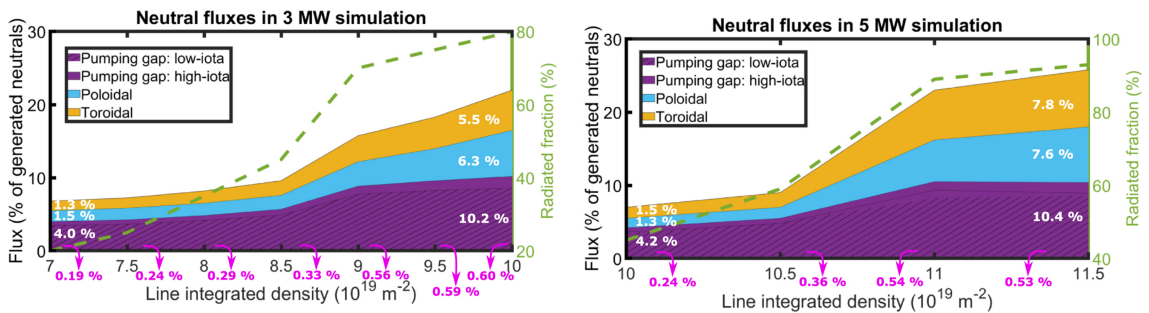


Figure 29: Neutral particle fluxes evaluated with EMC3-Eirene under attached and detached conditions [41].

On the basis of these simulations, the values obtained with EMC3-Eirene are about a factor of 6-15 larger than the experimental value. However, a direct comparison of these values with the experimental value of Wenzel et al. is not expedient, since the plasma parameters are different. Especially during high impurity radiation scenarios, the flux to the sub-divertor increases due to reduced reionisation near the targets [26].

4.10 Improvement possibilities

In the following section, possible improvements of the presented simulation are outlined. These include a higher complexity of the simulated geometry, a more accurate description of the physical processes and the possibility of automation.

Referring to the increased complexity of the simulated geometry, it is favourable to simulate a full module of W7-X and to include a simplified model of the sub-divertor region. This extended simulation would account for different sub-divertor outfluxes with varying divertor geometries and allow straightforward validation of the COMSOL simulation with the measured sub-divertor neutral gas pressures. However, this increase in complexity has so far been hindered by the limitation to single, non-intersecting Kisslinger files, as described in Section 4.4.

Therefore, a more sophisticated approach for the mesh generation needs to be developed. Two possible solutions are conceivable. The first is to develop a code that generates a volume mesh of the torus with cavities in the shape of the simulated components. This approach allows direct simulation on the imported mesh and the components do not need to be converted into COMSOL native geometry files.

The preferred option is to develop a more refined code that converts Kisslinger meshes into STEP files. The intersection of the simulated components can then be performed more efficiently using CAD software. The file format conversion could be achieved by interpreting Kisslinger meshes as Fourier spectra, which can be converted to STEP surfaces using CadQuery.

There are several possibilities for including additional physical processes in the simulation that have not yet been considered. Firstly, COMSOL allows not only the deterministic calculation of free molecular flows, but also the deterministic calculation of transitional flows using the lattice Boltzmann method. This would extend the neutral particle transport simulation to account for neutral-neutral collisions. First

attempts failed due to excessive computational effort.

Two processes resulting from plasma-neutrals interaction strongly influence the neutral particle transport. The first is the reionisation of particles in the SOL, and the second is the momentum transfer between incidenting ions and neutral particles, which tends to retain the neutrals close to the divertor targets [26]. The reionisation of particles in the SOL could be included in the simulation by modelling porous surfaces perpendicular to the SOL magnetic field. These surfaces would be partially permeable and partially absorptive to provide a reionisation particle sink. In addition, a coupling of the amount of absorbed particles at the porous SOL surfaces to the neutral particle source could include divertor plugging in the COMSOL simulation. The effect of momentum transfer could be considered by coupling the incidenting molecular flux at a finite surface element to the emission probability distribution used in the AC method. At higher flux densities, the probability of particles emitting at lower angles should be higher. These approaches could allow the effects of plasma-neutrals interaction to be included in the COMSOL simulation without actually modelling the plasma.

Of particular interest is an automated coupling of EMC3-Lite and the neutral particle transport simulation. This combined code would take only the Kisslinger meshes as input and quantify the heat deposition at the targets and the neutral particle transport. However, in COMSOL it is particularly difficult to automatically apply boundary conditions to a changing geometry. One possible approach is the standalone implementation of the AC method to the output of EMC3-Lite. This could allow automated transport optimisation of target geometries. Similar approaches for automated heat load optimisation are described by Davies et al. [57] and Liu et al. [58].

5 Summary

The objective of this thesis was to implement a simplified neutral particle transport simulation to shorten the design iterations of new divertor target geometries for W7-X. For the current W7-X divertor, its primary function - the particle exhaust capability - has only been a secondary design criterion. So far, the neutral particle transport could only be simulated laboriously using EMC3-Eirene.

For this purpose, a neutral particle source on the divertor targets was derived from the heat deposition calculated with the simplified plasma edge code EMC3-Lite. The resulting neutral gas dynamics are calculated in COMSOL using the AC method under the key assumption that the neutrals do not interact with plasma particles in the SOL or with other neutrals. The simulation has been performed on simplified geometries used in EMC3-Eirene simulations. The simulated components are the divertor targets, baffles, heat shields, pumping gap covers and the LCFS. The sub-divertor is not yet included. The different file requirements for EMC3-Eirene and COMSOL demanded the development of several codes to edit and convert Kisslinger files. Included particle sinks are the reionisation of particles in the main plasma, the flux to the sub-divertor and particles leaving the divertor region. Additionally, the sub-divertor outflux is taken into account. The simulation was performed for the standard, high-iota and high-mirror configurations and the particle sinks and the wall contribution to neutral particle transport were quantified. These values and the qualitative visualisation of the particle distribution match the intuitive expectations. Whilst a comprehensive validation of the simulation is still pending, a first comparison with experimental and EMC3-Eirene values shows good agreement.

Future efforts should focus on improving the simulation as described in Section 4.10. The starting point will be the inclusion of the sub-divertor in the simulated geometry and the development of a more sophisticated meshing approach. In parallel to this improvement, new target geometries for future divertor concepts will be elaborated whose particle exhaust can be quantified with the presented simulation. It might be advantageous to include a simple transport term in the generation of the target geometries, e.g. the average orientation of the Kisslinger elements with respect to the plasma core.

References

- [1] World Meteorological Organization, ed. *State of the Global Climate 2023*. United Nations, 2024. ISBN: 978-92-63-11347-4. URL: <https://www.un-ilibrary.org/content/books/9789263113474>.
- [2] Energy Institute, ed. *Statistical Review of World Energy 2024*. 73rd ed. 2024. ISBN: 978-1-78725-408-4.
- [3] International Atomic Energy Agency. *World Fusion Outlook 2023*. Vienna: IAEA, 2023. DOI: 10.61092/iaea.ehyw-jq1g.
- [4] Max-Planck-Institut für Plasmaphysik, ed. *Nuclear fusion: European joint experiment achieves energy record*. Accessed: 18.09.2024. URL: <https://www.ipp.mpg.de/5405892>.
- [5] Guido van Oost, ed. *Fundamentals of magnetic fusion technology*. Vienna: International Atomic Energy Agency, 2023. ISBN: 978-92-0-110721-3.
- [6] EUROfusion, ed. *European Research Roadmap to the Realisation of Fusion Energy*. Garching, 2018. ISBN: 978-3-00-061152-0.
- [7] Max-Planck-Institut für Plasmaphysik, ed. *Was der neue ITER-Zeitplan bedeutet*. Accessed: 18.09.2024. URL: <https://www.ipp.mpg.de/5434912>.
- [8] Daniel Clery. “Giant fusion project in big trouble”. In: *Science* 385, Issue 6704 (2024).
- [9] Fusion Industry Association, ed. *The global fusion industry in 2024*. Washington, DC, 2024.
- [10] Max-Planck-Institut für Plasmaphysik, ed. *What is nuclear fusion?* Accessed: 12.09.2024. URL: <https://www.ipp.mpg.de/15047/kernfusion>.
- [11] Edward Morse. *Nuclear Fusion*. Cham: Springer International Publishing, 2018. ISBN: 978-3-319-98171-0. DOI: 10.1007/978-3-319-98171-0.
- [12] Michael Kaufmann. *Plasmaphysik und Fusionsforschung*. Wiesbaden: Springer Fachmedien Wiesbaden, 2013. ISBN: 978-3-658-03238-8. DOI: 10.1007/978-3-658-03239-5.
- [13] Samuel E. Wurzel and Scott C. Hsu. “Progress toward fusion energy breakeven and gain as measured against the Lawson criterion”. In: *Physics of Plasmas* 29.6 (2022). ISSN: 1070-664X. DOI: 10.1063/5.0083990.
- [14] A. B. Zylstra et al. “Experimental achievement and signatures of ignition at the National Ignition Facility”. In: *Physical review. E* 106.2-2 (2022), p. 025202. DOI: 10.1103/PhysRevE.106.025202.
- [15] F. A. Khan. “On Tsar Bomba—the most powerful nuclear weapon ever tested”. In: *Physics Education* 56.1 (2021), p. 013002. DOI: 10.1088/1361-6552/abbcbc.

- [16] Ulrich Stroth. *Plasmaphysik: Phänomene, Grundlagen und Anwendungen*. Berlin, Heidelberg: Springer Berlin Heidelberg, 2017. ISBN: 978-3-662-55235-3.
- [17] Eric G. Blackman. “On deriving flux freezing in magnetohydrodynamics by direct differentiation”. In: *European Journal of Physics* 34.2 (2013), pp. 489–494. DOI: 10.1088/0143-0807/34/2/489.
- [18] Yuhong Xu. “A general comparison between tokamak and stellarator plasmas”. In: *Matter and Radiation at Extremes* 1.4 (2016), pp. 192–200. ISSN: 2468-2047. DOI: 10.1016/j.mre.2016.07.001.
- [19] R. König et al. “The divertor program in stellarators”. In: *Plasma Physics and Controlled Fusion* 44.11 (2002), pp. 2365–2422. DOI: 10.1088/0741-3335/44/11/306.
- [20] Thierry Kremeyer et al. “Analysis of hydrogen fueling, recycling, and confinement at Wendelstein 7-X via a single-reservoir particle balance”. In: *Nuclear Fusion* 62.3 (2022), p. 036023. DOI: 10.1088/1741-4326/ac4acb.
- [21] Prachai Norajitra. “Divertor development for a future fusion power plant”. Zugl.: Karlsruhe, Karlsruher Inst. für Technologie, Diss., 2011. Karlsruhe: KIT Scientific Publishing, 2011.
- [22] H. Greuner et al. “Final design of W7-X divertor plasma facing components—tests and thermo-mechanical analysis of baffle prototypes”. In: *Fusion Engineering and Design* 66-68 (2003), pp. 447–452. ISSN: 09203796. DOI: 10.1016/S0920-3796(03)00193-5.
- [23] Salah El-Din El-Morshedy. “Thermal-hydraulic simulation of ITER tungsten divertor monoblock for loss of flow transient”. In: *Nuclear Materials and Energy* 38 (2024), p. 101616. ISSN: 23521791. DOI: 10.1016/j.nme.2024.101616.
- [24] A. Q. Kuang et al. “Divertor heat flux challenge and mitigation in SPARC”. In: *Journal of Plasma Physics* 86.5 (2020). DOI: 10.1017/S0022377820001117.
- [25] Nikolaos Perakis, Lukas Preis, and Oskar J. Haidn. “Wall Heat Flux Evaluation in Regeneratively Cooled Rocket Thrust Chambers”. In: *Journal of Thermophysics and Heat Transfer* 35.1 (2021), pp. 127–141. DOI: 10.2514/1.T6056.
- [26] Y. Feng et al. “Understanding detachment of the W7-X island divertor”. In: *Nuclear Fusion* 61.8 (2021), p. 086012. DOI: 10.1088/1741-4326/ac0772.
- [27] Jan Willem Coenen. “The influence of the dynamic ergodic divertor on the radial electric field at the tokamak TEXTOR”. Zugl.: Düsseldorf, Univ., Diss, 2009. Jülich Forschungszentrum, 2009.
- [28] Peter C. Stangeby. *The plasma boundary of magnetic fusion devices*. Bristol: Institute of Physics Publishing, 2000. ISBN: 978-0750305594.
- [29] G. Grieger, H. Renner, and H. Wobig. “Wendelstein stellarators”. In: *Nuclear Fusion* 25.9 (1985), pp. 1231–1242. DOI: 10.1088/0029-5515/25/9/040.

- [30] Y. Feng et al. “Physics of island divertors as highlighted by the example of W7-AS”. In: *Nuclear Fusion* 46.8 (2006), pp. 807–819. DOI: 10.1088/0029-5515/46/8/006.
- [31] Y. Feng et al. “3D Edge Modeling and Island Divertor Physics”. In: *Contributions to Plasma Physics* 44.1-3 (2004), pp. 57–69. ISSN: 0863-1042. DOI: 10.1002/ctpp.200410009.
- [32] Allen H. Boozer. “Physics of magnetically confined plasmas”. In: *Reviews of Modern Physics* 76.4 (2005), pp. 1071–1141. DOI: 10.1103/RevModPhys.76.1071.
- [33] R. C. Wolf et al. “Major results from the first plasma campaign of the Wendelstein 7-X stellarator”. In: *Nuclear Fusion* 57.10 (2017), p. 102020. DOI: 10.1088/1741-4326/aa770d.
- [34] G. Grieger et al. “Physics optimization of stellarators”. In: *Physics of Fluids B: Plasma Physics* 4.7 (1992), pp. 2081–2091. ISSN: 0899-8221. DOI: 10.1063/1.860481.
- [35] V. Erckmann et al. “The W7-X project: scientific basis and technical realization”. In: *17th IEEE/NPSS Symposium Fusion Engineering*. 1998, pp. 40–48. ISBN: 0-7803-4226-7. DOI: 10.1109/FUSION.1997.685662.
- [36] T. Klinger et al. “Performance and properties of the first plasmas of Wendelstein 7-X”. In: *Plasma Physics and Controlled Fusion* 59.1 (2017), p. 014018. DOI: 10.1088/0741-3335/59/1/014018.
- [37] H. Renner et al. “The capabilities of steady state operation at the stellarator W7-X with emphasis on divertor design”. In: *Nuclear Fusion* 40.6 (2000), pp. 1083–1093. DOI: 10.1088/0029-5515/40/6/306.
- [38] Thomas Sunn Pedersen et al. “First results from divertor operation in Wendelstein 7-X”. In: *Plasma Physics and Controlled Fusion* 61.1 (2019), p. 014035. DOI: 10.1088/1361-6587/aaec25.
- [39] J. Boscary et al. “Conceptual design of the next generation of W7-X divertor W-target elements”. In: *Fusion Engineering and Design* 192 (2023), p. 113629. ISSN: 09203796. DOI: 10.1016/j.fusengdes.2023.113629.
- [40] V. Haak et al. “Overview over the neutral gas pressures in Wendelstein 7-X during divertor operation under boronized wall conditions”. In: *Plasma Physics and Controlled Fusion* 65.5 (2023), p. 055024. DOI: 10.1088/1361-6587/acc8fb.
- [41] Dieter Boeyaert et al. “Analysis of the neutral fluxes in the divertor region of Wendelstein 7-X under attached and detached conditions using EMC3-EIRENE”. In: *Plasma Physics and Controlled Fusion* 66.1 (2024), p. 015005. DOI: 10.1088/1361-6587/ad0e22.

- [42] N. Marquardt. *Introduction to the principles of vacuum physics*. Ed. by Institute for Accelerator Physics and Synchrotron Radiation, University of Dortmund. Dortmund, 1999. DOI: 10.5170/CERN-1999-005.1.
- [43] Austin Chambers. *Modern vacuum physics*. Masters series in physics and astronomy. Boca Raton: Chapman & Hall/CRC, 2005. ISBN: 0-8493-2438-6.
- [44] Yangyu Guo and Moran Wang. “Phonon hydrodynamics and its applications in nanoscale heat transport”. In: *Physics Reports* 595 (2015), pp. 1–44. ISSN: 03701573. DOI: 10.1016/j.physrep.2015.07.003.
- [45] Carl L. Yaws. *Transport Properties of Chemicals and Hydrocarbons*. Elsevier, 2014. ISBN: 9780323286589. DOI: 10.1016/C2013-0-12644-X.
- [46] Franck Celestini and Fabrice Mortessagne. “Cosine law at the atomic scale: toward realistic simulations of Knudsen diffusion”. In: *Physical review. E, Statistical, nonlinear, and soft matter physics* 77.2 Pt 1 (2008), p. 021202. ISSN: 1539-3755. DOI: 10.1103/PhysRevE.77.021202.
- [47] COMSOL, ed. *Molecular Flow Module User’s Guide*. Last accessed: 11.11.2024. URL: <https://doc.comsol.com/5.3/doc/com.comsol.help.molec/MolecularFlowModuleUsersGuide.pdf>.
- [48] Liangliang Cao et al. “Direct numerical simulation of supersonic nanoparticles flow in free-molecule regime using the angular coefficient method”. In: *Physics of Fluids* 36.2 (2024). ISSN: 1070-6631. DOI: 10.1063/5.0175166.
- [49] Y. Feng et al. “Recent Improvements in the EMC3–Eirene Code”. In: *Contributions to Plasma Physics* 54.4-6 (2014), pp. 426–431. ISSN: 0863-1042. DOI: 10.1002/ctpp.201410092.
- [50] Y. Feng. “Review of magnetic islands from the divertor perspective and a simplified heat transport model for the island divertor”. In: *Plasma Physics and Controlled Fusion* 64.12 (2022), p. 125012. DOI: 10.1088/1361-6587/ac9ed9.
- [51] Hailin Bi et al. “Simulation study of effective pumping speed of divertor pumping system for CFETR with COMSOL Multiphysics”. In: *Fusion Engineering and Design* 194 (2023), p. 113916. ISSN: 09203796. DOI: 10.1016/j.fusengdes.2023.113916.
- [52] K-U Riemann. “The Bohm criterion and sheath formation”. In: *Journal of Physics D: Applied Physics* 24.4 (1991), pp. 493–518. DOI: 10.1088/0022-3727/24/4/001.
- [53] S. Varoutis et al. “Numerical simulation of neutral gas dynamics in the W7-X sub-divertor”. In: *Nuclear Fusion* 64.7 (2024), p. 076011. DOI: 10.1088/1741-4326/ad49b5.

- [54] U. Wenzel et al. “Gas exhaust in the Wendelstein 7-X stellarator during the first divertor operation”. In: *Nuclear Fusion* 63.9 (2023), p. 099501. DOI: 10.1088/1741-4326/aceb78.
- [55] G. A. Wurden et al. “A high resolution IR/visible imaging system for the W7-X limiter”. In: *The Review of scientific instruments* 87.11 (2016), p. 11D607. DOI: 10.1063/1.4960596.
- [56] Uwe Wenzel et al. “Performance of new crystal cathode pressure gauges for long-pulse operation in the Wendelstein 7-X stellarator”. In: *The Review of scientific instruments* 90.12 (2019), p. 123507. DOI: 10.1063/1.5121203.
- [57] Robert Davies et al. “A semi-automated algorithm for designing stellarator divertor and limiter plates and application to HSX”. In: *Nuclear Fusion* 64.12 (2024), p. 126044. DOI: 10.1088/1741-4326/ad8017.
- [58] B. Liu et al. “A universal target plate design scheme for stellarators: theoretical basis and its application to heat load control”. In: *Nuclear Fusion* 65.1 (2025), p. 016023. DOI: 10.1088/1741-4326/ad8edc.

List of Figures

1	Progress of fusion research indicated by the triple product [13].	4
2	Schematic of a toroid [Own graphic].	5
3	Tokamak (left) and stellarator (right) field coils and plasma configuration [Graphics: Max Planck Institute for Plasma Physics].	6
4	Limiter (left) and single-null divertor (right) configuration [27].	10
5	W7-AS island divertor configuration: the poloidal cross section shows nine island cross sections, six of which are intersected by divertor targets [30].	13
6	Cutaway diagram visualising the structure of W7-X; a sketched human serves as a size comparison [36].	16
7	Rendering of the divertor units (black) surrounding the LCFS (orange) [38].	17
8	Image of the inside of the plasma vessel with the divertor targets highlighted in red, the strikeline (blue) and the magnetic flux surfaces (green) [Graphic: Daniel Böckenhoff, Max Planck Institute for Plasma Physics].	18
9	CAD rendering of one divertor unit showing the PFCs, the large and small pumping gaps and the ports connected to the sub-divertor [40].	19
10	Scheme of the simplified two-dimensional calculation of particles entering the sub-divertor [Own graphic].	23
11	Simplified visualisation of the AC method [Own graphic].	25
12	Schematic of a Kisslinger mesh of size ($n_t = 5$, $n_p = 4$) with the specified coordinate system [Own graphic].	29
13	Coloured COMSOL rendering of the low-iota section [Own graphic].	30
14	Coloured COMSOL rendering of the middle and high-iota sections [Own graphic].	31
15	Transparent COMSOL rendering of the entire simulated geometry [Own graphic].	32
16	Deformations in Kisslinger files [Own graphic].	32
17	Waveforms in converted Kisslinger file [Own graphic].	33
18	Combined Kisslinger mesh [Own graphic].	34
19	Final triangular mesh used in the simulation [Own graphic].	34
20	Relative deviation and computing time plotted against the average element size [Own graphic].	35
21	Interpolated flux density scalar field for the horizontal divertor in the low-iota section (left) and the neutral particle source in COMSOL for the standard configuration (right) [Own graphic].	38
22	Temperature distribution on the divertor targets during an average discharge [Graphic: Yu Gao, Max Planck Institute for Plasma Physics].	39

23	Neutral particle source for the standard configuration [Own graphic].	42
24	Calculated neutral particle flux distribution in the standard configuration [Own graphic].	42
25	Neutral particle source for the high-iota configuration [Own graphic].	44
26	Calculated neutral particle flux distribution in the high-iota configuration [Own graphic].	44
27	Neutral particle source for the high-mirror configuration [Own graphic].	46
28	Calculated neutral particle flux distribution in the high-mirror configuration. [Own graphic].	46
29	Neutral particle fluxes evaluated with EMC3-Eirene under attached and detached conditions [41].	48

List of Tables

1	Calculated neutral particle sinks in the standard configuration.	43
2	Contribution of wall components to neutral particle transport in the standard configuration.	43
3	Calculated neutral particle sinks in the high-iota configuration.	45
4	Contribution of wall components to neutral particle transport in the high-iota configuration.	45
5	Calculated neutral particle sinks in the high-mirror configuration. . .	47
6	Contribution of wall components to neutral particle transport in the high-mirror configuration.	47